Error analysis of pressure reconstruction from discrete velocities

Rodolfo Araya, Cristobal Bertoglio, Cristian Cárcamo, David Nolte, Sergio Uribe

Error analysis of pressure reconstruction from discrete velocities

Rodolfo Araya[a], Cristóbal Bertoglio[b], Cristian Cárcamo[a,b], David Nolte[b,c], Sergio Uribe[d]

[a] *Departamento de Ingeniería Matemática & CI^{2}MA, Universidad de Concepción, Chile*
[b] *Bernoulli Institute, University of Groningen, The Netherlands*
[c] *Department of Fluid Dynamics, Technical University of Berlin, Germany*
[d] *Center of Biomedical Imaging, Pontificia Universidad Católica, Chile*

Abstract

Magnetic Resonance Imaging allows to measure the three-dimensional velocity field in blood flows. Therefore, several methods have been proposed to reconstruct the pressure field from such measurements using the incompressible Navier-Stokes equations. However, those measurements are obtained at limited spatial resolution given by the voxel dimensions in the image. Therefore, the velocity entering to the right-hand-side corresponds to a piecewise linear interpolation of the exact velocity.
In this work we propose a strategy for convergence analysis of state-of-the-art pressure reconstruction methods. The methods analyzed are the the so called Pressure Poisson Estimator (PPE) and Stokes Estimator (STE). In the theoretical error analysis, we show that many terms of different convergence order appear. However, numerical results, show in academic examples that only the PPE may profit of increasing the polynomial order, and that the STE presents a higher accuracy than the PPE.
Additionally, we compare the pressure estimation methods on real MRI data, assessing the impact of different spatial resolutions and polynomial degree on each of the methods. Here, the results are aligned with the academic test cases in terms of sensitivity to polynomial order and that the STE shows to be potentially more accurate when compared to reference pressure measurements.

Email addresses: rodolfo.araya@udec.cl (Rodolfo Araya), c.a.bertoglio@rug.nl (Cristóbal Bertoglio), c.e.carcamo@rug.nl (Cristian Cárcamo), dajuno@riseup.net (David Nolte), suribe@uc.cl (Sergio Uribe)

1. Introduction

The intra-arterial spatial distribution of the blood pressure can be measured by means of catheterization [2]. This technique consists in inserting a catheter equipped with a pressure transducer into the vasculature of the patient and manoeuvring it, under local anaesthesia and guided by fluoroscopy, to the location of interest. Although it is the 'clinical gold standard' for pressure quantification, the invasive nature of the method is associated with a risk of complications [27, 25, 14]. Given that there are recommendations to avoid its use [23], to compute the pressure difference from measured flow fields is strongly preferred.
Time-resolved 3D velocity encoded magnetic resonance imaging, or *4D flow MRI*, offers measuring the complete 3D velocity field within a region of interest [11, 19]. The measured velocities can then be inserted in the linear momentum balance of the incompressible Navier-Stokes equations (NSE) and the velocity terms laid in the right-hand-side while the pressure holds as an unknown, i.e.,for a given measurement of the velocity $\boldsymbol{u}$, the pressure gradient ∇p is found by solving:

$$\nabla p = -\boldsymbol{f}_{\boldsymbol{u}} \text{ in } \Omega \tag{1}$$

with $\Omega \subset \mathbb{R}^d$ and $\boldsymbol{f}_{\boldsymbol{u}} := (\boldsymbol{u} \cdot \nabla)\boldsymbol{u} - \nu\Delta\boldsymbol{u}.$, where the proper function spaces will be defined for each of the methods throughout the article. An example of pressure map estimation from real 4D Flow MRI data is shown in Figure 1.

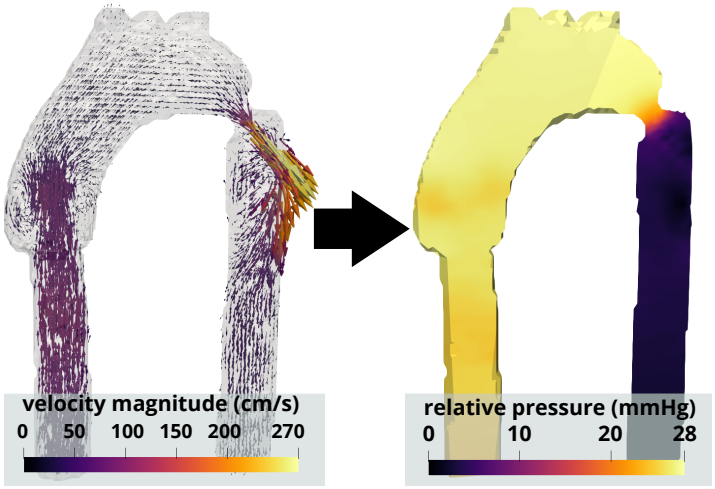

Figure 1: Pressure map estimation from in an experimental phantom of a thoraxic aorta [21], adapted and reprinted from [13]: Left: The 4D Flow MRI velocity measurements. Right: Relative pressure map computed from velocity data. Shown: cuts through roughly the center of the vessels.

In practice, and as it can be appreciated in Figure 1-Left, those measurements are obtained at limited spatial resolution –given by the voxel size in the image – and therefore the velocity entering to the right-hand-side corresponds to an interpolated version of the exact velocity. Therefore, there is not a unique numerical approach to compute the reconstructed pressures. A review and preliminary numerical comparison of methods can be found in [3]. Among those methods, only a few can compute pressure fields and not just averaged pressure differences between two locations.
The first one is the so-called Pressure Poisson Estimator (PPE) [6, 18] and it consists of applying the divergence to the NSE obtaining a pressure Poisson equation, similarly as it is used in projection methods [9]. However, the original PPE method cannot include the viscous contribution to the pressure gradient at the level of accuracy of the measured data. Therefore, recently in [16] the PPE method was modified by adding a boundary term with the viscous contribution.
Another more modern method corresponds to the Stokes Estimator (STE) was reported in [22]. The STE consists in adding to the NSE the Laplacian of an artificial incompressible velocity field with null trace

leading to a linear Stokes problem for both pressure and artificial velocity fields. Such artificial velocity is supposed to be zero for perfect velocity measurements. The STE has shown more accurate results than the PPE in numerically simulated data [22, 3] and in real phantom and patient data [13]. However, the STE method is considerably more expensive computationally than the PPE.

To the best of the authors' knowledge, neither a mathematical convergence analysis of both PPE and STE methods or a comparison among discretization schemes for each of the methods has been reported.

Therefore, the purpose of this work is to propose a strategy for performing a priori error analysis and applied it to the PPE and STE methods. The strategy is based on the splitting of the solution in two components and adding their contributions to the overall error. Moreover, for both methods we studied different discretization strategies in order to verify the theoretical analysis and give insights on the cost-effectiveness of each approach. In order to assess the impact of discretizations on each of the methods, calculations of pressure fields based on experimental MRI data are also included.

The remainder of this work is organized as follows. In Section 2 we present and analyze the PPE method in the standard and modified variants using Continuos Galerkin approaches. Section 3 introduces the STE and analyzes the classical Taylor-Hood and a tailored PSPG discretization. Then, in Section 4 we show numerical results using three known analytical solutions for the NSE, confirming the a priori error analysis. In Section 5 the methods are assessed under different spatial resolutions and polynomial degree on experimental MRI data. Finally, in Section 6 we draw some interpretation of the results and give recommendations for the use of these methods.

2. The Poisson Pressure Estimator

2.1. The continuous problem

The Poisson Pressure Estimator (PPE) consists in obtaining the pressure from the classical Navier-Stokes equation by mean a Poisson equation. That is, by applying the divergence operator on Equation (1) one gets

$$\begin{cases} -\Delta q & = \nabla \cdot \boldsymbol{f_u}, \quad \text{in } \Omega \\ -\frac{\partial q}{\partial \boldsymbol{n}} & = \boldsymbol{f_u} \cdot \boldsymbol{n}, \quad \text{on } \partial\Omega \\ \int_\Omega q\, dx & = 0, \end{cases} \tag{2}$$

with $\boldsymbol{n}$ the outward normal vector of $\partial\Omega$. We will make use of the function spaces $\boldsymbol{H} := [H^1(\Omega)]^d, \mathbf{V} := [H_0^1(\Omega)]^d$ and

$$\boldsymbol{H}_j := \begin{cases} \{\boldsymbol{v} \in \boldsymbol{H} : \Delta \boldsymbol{v} \in [L^2(\Omega)]^d\} & \text{if } j = 1 \\ \{\boldsymbol{v} \in \boldsymbol{H} : \nabla \times (\nabla \times \boldsymbol{u}) \in [L^2(\Omega)]^d\} & \text{if } j = 2 \end{cases}$$

$$Q_j := \begin{cases} \{r \in H^1(\Omega) : \int_\Omega r dx = 0\} & \text{if } j = 1 \\ \{r \in H^1(\Omega) : \boldsymbol{n} \cdot \operatorname{curl} r \in L^2(\partial\Omega) \text{ and } \int_\Omega r\, dx = 0\} & \text{if } j = 2 \end{cases}$$

Assuming $\boldsymbol{u} \in \boldsymbol{H}_j$, the weak formulation of the (2) is given by: Find $q \in Q_j$ such that

$$\mathcal{A}(q, r) = F_{\boldsymbol{u}}^j(r), \quad \forall\, r \in Q_j, \tag{3}$$

where $\mathcal{A}(q, r) = (\nabla q, \nabla r)_\Omega$ and

$$F_{\boldsymbol{u}}^j(r) = -((\boldsymbol{u} \cdot \nabla)\boldsymbol{u}, \nabla r)_\Omega + \delta_{1j}(\nu \Delta \boldsymbol{u}, \nabla r)_\Omega + \delta_{2j}\langle \boldsymbol{n} \times \nabla r, \nu \nabla \times \boldsymbol{u}\rangle_{\partial\Omega}, \tag{4}$$

where δ_{ij} is the Kronecker delta. We refer to Standard-PPE if $j = 1$ and Modified-PPE if $j = 2$ [16].

The uniqueness of the solution of Problem (3) follows from the Lax-Milgram lemma [7]. Indeed, the coercivity of the left-side is straightforward. The continuity of $F_{\boldsymbol{u}}^j$ is obtained thanks to the identity

$$-(\nabla r, \nu \nabla \times (\nabla \times \boldsymbol{u}))_\Omega = \langle \boldsymbol{n} \times \nabla r, \nu \nabla \times \boldsymbol{u}\rangle_{\partial\Omega}, \tag{5}$$

and then

$$|F_{\boldsymbol{u}}^j(r)| \leq (\|(\boldsymbol{u} \cdot \nabla)\boldsymbol{u}\|_{0,\Omega} + \delta_{1j}\nu\|\Delta \boldsymbol{u}\|_{0,\Omega} + \delta_{2j}\nu\|\nabla \times (\nabla \times \boldsymbol{u})\|_{0,\Omega})|r|_{1,\Omega}$$

2.2. Continuous Galerkin discretizations

The finite element spaces for the pressure approximation and velocity interpolation are:

$$\begin{aligned} Q_{jh} &:= \{q_h \in Q_j : q_h|_K \in \mathcal{P}_k(K) \quad \forall K \in \mathcal{T}_h\}, \\ \boldsymbol{H}_{jh} &:= \{v_h \in \boldsymbol{H}_j : v_h|_K \in \mathcal{P}_1(K) \quad \forall K \in \mathcal{T}_h\}. \end{aligned}$$

We will also consider the Lagrange interpolation operator $\mathcal{J}_h : Q_j \cap H^{k+1}(\Omega) \to Q_{jh}$ and $\mathcal{L}_h : \boldsymbol{H}_j \cap [H^2(\Omega)]^d \to H_{jh}$ such that:

$$\begin{aligned} |q - \mathcal{J}_h q|_{m,\Omega} &\leq a_k\, h^{k+1-m}|q|_{k+1,\Omega}, \qquad \forall\, q \in H^{k+1}(\Omega),\ 0 \leq m \leq k+1. \\ |\boldsymbol{v} - \mathcal{L}_h \boldsymbol{v}|_{m,\Omega} &\leq a_k\, h^{2-m}|\boldsymbol{v}|_{2,\Omega}, \qquad \forall\, \boldsymbol{v} \in H^2(\Omega),\ 0 \leq m \leq 2. \end{aligned} \tag{6}$$

Thus, the Galerkin scheme associated with the continuous variational formulation (3) reads as follows: Find $q_h \in Q_{jh}$ such that

$$\mathcal{A}(q_h, r_h) := F^j_{\boldsymbol{u}_h}(r_h) \quad \forall\, r_h \in Q_{jh}, \tag{7}$$

with

$$F^j_{\boldsymbol{u}_h}(r_h) = -((\mathcal{L}_h\boldsymbol{u}\cdot\nabla)\mathcal{L}_h\boldsymbol{u}, \nabla r_h)_\Omega + \delta_{2j} \sum_{F\in\mathcal{E}_h\cap\partial\Omega} \langle \boldsymbol{n}\times\nabla r_h, \nu\nabla\times\mathcal{L}_h\boldsymbol{u}\rangle_F, \tag{8}$$

According to discrete Lax-Milgram Theorem (Generalized Lax-Milgram for $j = 2$), Problem (7) has a unique solution $q_h \in Q_{jh}$.

Remark 1. *Note that from the definitions* (4) *and* (8) *we can assure that the problem* (7) *is not a Galerkin scheme of the continuous problem* (3)*. Indeed, the scheme is not consistent.*

The strategy to prove convergence is to use the known Strang's lemma for conformal and non-consistent cases.
In order to prove the convergence theorems, let us state the next result.

Lemma 1. *Let us assume that $\boldsymbol{u} \in H^2(\Omega)$. Then,*

$$\|(\boldsymbol{u}\cdot\nabla)\boldsymbol{u} - (\mathcal{L}_h\boldsymbol{u}\cdot\nabla)\mathcal{L}_h\boldsymbol{u}\|_{0,\Omega} \leq \tilde{C}(a_1 + a_2 C_I)h|\boldsymbol{u}|_{2,\Omega}\|\boldsymbol{u}\|_{2,\Omega}. \tag{9}$$

with a_1, a_2 the error interpolation constants, $\tilde{C}$ is an injection constant and C_I an inverse inequality constant.

Proof. Using properties of interpolation given by (6) and Young inequality we obtain

$$\begin{aligned} \|(\boldsymbol{u}\cdot\nabla)\boldsymbol{u} - (\mathcal{L}_h\boldsymbol{u}\cdot\nabla)\mathcal{L}_h\boldsymbol{u}\|_{0,\Omega} \leq& \|(\boldsymbol{u}\cdot\nabla)(\boldsymbol{u} - \mathcal{L}_h\boldsymbol{u})\|_{0,\Omega} + \|((\boldsymbol{u} - \mathcal{L}_h\boldsymbol{u})\cdot\nabla)\mathcal{L}_h\boldsymbol{u}\|_{0,\Omega} \\ \leq& |\boldsymbol{u} - \mathcal{L}_h\boldsymbol{u}|_{1,\Omega}\|\boldsymbol{u}\|_{\infty,\Omega} + \|\nabla\mathcal{L}_h\boldsymbol{u}\|_{\infty,\Omega}\|\boldsymbol{u} - \mathcal{L}_h\boldsymbol{u}\|_{0,\Omega} \\ \leq& a_1 h|\boldsymbol{u}|_{2,\Omega}\tilde{C}\|\boldsymbol{u}\|_{2,\Omega} + C_I h^{-1}\|\mathcal{L}_h\boldsymbol{u}\|_{\infty,\Omega}a_2 h^2|\boldsymbol{u}|_{2,\Omega} \\ \leq& \tilde{C}a_1 h|\boldsymbol{u}|_{2,\Omega}\|\boldsymbol{u}\|_{2,\Omega} + a_2 C_I h\|\boldsymbol{u}\|_{\infty,\Omega}|\boldsymbol{u}|_{2,\Omega} \\ \leq& \tilde{C}a_1 h|\boldsymbol{u}|_{2,\Omega}\|\boldsymbol{u}\|_{2,\Omega} + a_2\tilde{C}\,C_I h\|\boldsymbol{u}\|_{2,\Omega}|\boldsymbol{u}|_{2,\Omega} \\ =& \tilde{C}(a_1 + a_2 C_I)h|\boldsymbol{u}|_{2,\Omega}\|\boldsymbol{u}\|_{2,\Omega} \end{aligned} \tag{10}$$

■

Lemma 2. *Assume that $\boldsymbol{u} \in \boldsymbol{H}_j \cap H^2(\Omega)^d$ if $j = 1$ and $\boldsymbol{u} \in \boldsymbol{H}_j$ with $\boldsymbol{u}\big|_{\partial\Omega} \in [H^2(\partial\Omega)]^d$ if $j = 2$. Then,*

$$\sup_{\substack{r_h\in Q_{jh}\\ r_h\neq 0}} \frac{|F^j_{\boldsymbol{u}}(r_h) - F^k_{\boldsymbol{u}_h}(r_h)|}{|r_h|_{1,\Omega}} \leq C_1 h|\boldsymbol{u}|_{2,\Omega}\|\boldsymbol{u}\|_{2,\Omega} + \delta_{1,j}\|\Delta\boldsymbol{u}\|_{0,\Omega} + \delta_{2,j}C_2\nu h^{1/2}|\boldsymbol{u}|_{2,\partial\Omega}$$

Proof.

$$\sup_{\substack{r_h\in Q_{jh}\\ r_h\neq 0}} \frac{|F^j_{\boldsymbol{u}}(r_h)-F^k_{\boldsymbol{u}_h}(r_h)|}{|r_h|_{1,\Omega}} \leq \|(\boldsymbol{u}\cdot\nabla)\boldsymbol{u}-(\mathcal{I}_h\boldsymbol{u}\cdot\nabla)\mathcal{I}_h\boldsymbol{u}\|_{0,\Omega}+\delta_{1,j}\|\Delta\boldsymbol{u}\|_{0,\Omega} + \delta_{2,j}\sup_{\substack{r_h\in Q_{jh}\\ r_h\neq 0}} \frac{\displaystyle\sum_{F\in\mathcal{E}_h\cap\partial\Omega}|\langle \boldsymbol{n}\times\nabla r_h, \nu\,\nabla\times(u-\mathcal{I}_h\boldsymbol{u})\rangle_{\partial\Omega}|}{|r_h|_{1,\Omega}}.$$

For the first term in above inequality we use Lemma 1 and for the third term we have

$$\frac{\displaystyle\sum_{F\in\mathcal{E}_h\cap\partial\Omega}|\langle \boldsymbol{n}\times\nabla r_h, \nu\,\nabla\times(u-\mathcal{I}_h\boldsymbol{u})\rangle_F|}{|r_h|_{1,\Omega}} \leq \frac{\displaystyle\sum_{F\in\mathcal{E}_h\cap\partial\Omega}\nu\,\|\nabla r_h\|_{0,F}\|\nabla\times(u-\mathcal{I}_h\boldsymbol{u})\|_{0,F}}{|r_h|_{1,\Omega}} \tag{11}$$

Now, thanks to [5, Lemma 1.46], we have

$$\|\nabla r_h\|_{0,F}\leq C_{tr}h_K^{-1/2}|r_h|_{1,K}, \tag{12}$$

where $C_{tr}=\left(\dfrac{(k+1)(k+2)}{2}\right)^{1/2}$ (see [26, Theorem 3]). Besides, from [20, Lemma 10.8] we get

$$\|\nabla\times(\boldsymbol{u}-\mathcal{I}_h\boldsymbol{u})\|_{0,F}\leq C_b|\boldsymbol{u}-\mathcal{I}_h\boldsymbol{u}|_{1,F}\leq C_b a_{2,I}\,h_K\,|\boldsymbol{u}|_{2,F}. \tag{13}$$

and then, from (11), (12) and (13) we arrive to

$$\frac{\displaystyle\sum_{F\in\mathcal{E}_h\cap\partial\Omega}|\langle \boldsymbol{n}\times\nabla r_h, \nu\,\nabla\times(u-\mathcal{I}_h\boldsymbol{u})\rangle_F|}{|r_h|_{1,\Omega}} \leq C_{tr}C_b\,a_{2,I}\,\nu\,h^{1/2}|\boldsymbol{u}|_{2,\partial\Omega},$$

being $C_2=C_{tr}\,C_b\,a_{2,I}$, which allows us arrive to the desired result, where $C_1=\tilde{C}(a_1+a_2C_I)$. ■

Finally, the next theorem holds.

Theorem 1 (Main Result I). *Let $q\in Q_j\cap H^{k+1}(\Omega)$ and $q_h\in Q_{jh}$ solutions of (3) and (7), respectively. In addition, we assume that $\boldsymbol{u}\in\boldsymbol{H}_j\cap[H^2(\Omega)]^d$ and $\boldsymbol{u}\in\boldsymbol{H}_j$ with $\boldsymbol{u}\big|_{\partial\Omega}\in[H^2(\partial\Omega)]^d$, for $j=1$ and $j=2$ respectively. Then,*

$$|q-q_h|_{1,\Omega}\leq\ a_kh^k|q|_{k+1,\Omega}+C_1h|\boldsymbol{u}|_{2,\Omega}\|\boldsymbol{u}\|_{2,\Omega}+\delta_{1,j}\|\Delta\boldsymbol{u}\|_{0,\Omega}+\delta_{2,j}C_2\nu h^{1/2}|\boldsymbol{u}|_{2,\partial\Omega}$$

with $k\geq 1$.

Proof. Thanks to the Strang's Lemma (see [7, Lemma 2.27]) we have that

$$|q-q_h|_{1,\Omega}\leq \sup_{\substack{r_h\in Q_{jh}\\ r_h\neq 0}}\frac{|F^j_{\boldsymbol{u}}(r_h)-F^j_{\boldsymbol{u}_h}(r_h)|}{|r_h|_{1,\Omega}}+2\inf_{r_h\in Q_{jh}}|q-r_h|_{1,\Omega}$$

The bound for the first term in the right-hand side follows directly from Lemma 2. For the second term, we will consider the interpolation operator, and then

$$\inf_{r_h\in Q_{jh}}|q-r_h|_{1,\Omega}\leq|q-\mathcal{J}_hq|_{1,\Omega}\leq a_kh^k|q|_{k+1,\Omega}$$

■

Corollary 1. *Let the hypothesis of Theorem 1 hold with Ω is convex polygonal domain. Then,*

$$\|q - q_h\|_{0,\Omega} \leq C_r\, a_k h^{k+1}|q|_{k+1,\Omega} + C_1\, C_p h|\boldsymbol{u}|_{2,\Omega}\|\boldsymbol{u}\|_{2,\Omega} + \delta_{1,j}\, C_p\|\Delta\boldsymbol{u}\|_{0,\Omega} + \delta_{2,j}\, C_2\, C_p\, \nu h^{1/2}|\boldsymbol{u}|_{2,\partial\Omega}$$

with C_r the regularity constant and $k \geq 1$.

Proof.
The proof starts taking $\tilde{q}_h \in Q_{jh}$ such that satisfy Equation (3). It follows from the triangle inequality that

$$\|q - q_h\|_{0,\Omega} \leq \|q - \tilde{q}_h\|_{0,\Omega} + \|\tilde{q}_h - q_h\|_{0,\Omega} \tag{14}$$

The bound estimation for $\|q - \tilde{q}_h\|_{0,\Omega}$ is obtained solving the problem

$$-\Delta r = q - \tilde{q}_h,$$

with the Dirichlet conditon zero and applying the known Aubin-Nitsche Lemma [7, Lemma 2.31] and interpolation properties leading to

$$\|q - \tilde{q}_h\|_{0,\Omega} \leq C_r h|q - \tilde{q}_h|_{1,\Omega} \leq C_r a_k h^{k+1}|q|_{k+1,\Omega}. \tag{15}$$

For the second term of the right-hand side in (14) we proceed as follows:

$$|\tilde{q}_h - q_h|_{1,\Omega} \leq \sup_{\substack{r_h \in Q_{jh} \\ r_h \neq 0}} \frac{\mathcal{A}(\tilde{q}_h - q_h, r_h)}{|r_h|_{1,\Omega}} \leq \sup_{\substack{r_h \in Q_{jh} \\ r_h \neq 0}} \frac{F^j_{\boldsymbol{u}}(r_h) - F^j_{\boldsymbol{u}_h}(r_h)}{|r_h|_{1,\Omega}}.$$

From Lemma 2 and Poincaré inequality, we get

$$\|\ \tilde{q}_h - q_h\|_{0,\Omega} \leq C_p|\tilde{q}_h - q_h|_{1,\Omega} \leq C_1\, C_p h|\boldsymbol{u}|_{2,\Omega}\|\boldsymbol{u}\|_{2,\Omega} + \delta_{1,j}\, C_p\|\Delta\boldsymbol{u}\|_{0,\Omega} + \delta_{2,j}\, C_2\, C_p\, \nu h^{1/2}|\boldsymbol{u}|_{2,\partial\Omega}. \tag{16}$$

Hence, the result is a direct consequence of the estimates (15) and (16).

■

3. The Stokes Estimator

3.1. The continuous problem

The STE consists then in adding the Laplacian of an incompressible auxiliary velocity $\boldsymbol{w} \in \mathbf{V}$ and to the left-hand side of (1):

$$\begin{aligned} -\Delta\boldsymbol{w} + \nabla q &= -\boldsymbol{f}_{\boldsymbol{u}} \quad \text{in } \Omega \\ \nabla \cdot \boldsymbol{w} &= 0 \quad \text{in } \Omega. \end{aligned} \tag{17}$$

Let us define the space $P = L^2_0(\Omega)$. Hence, we can define the weak problem of (17) as: *Find* $(\boldsymbol{w}, q) \in \mathbf{V} \times P$ *such that*

$$\mathcal{B}((\boldsymbol{w}, q), (\boldsymbol{v}, r)) = \mathcal{G}_{\boldsymbol{u}}(\boldsymbol{v}, r) \quad \forall (\boldsymbol{v}, r) \in \mathbf{V} \times P, \tag{18}$$

where

$$\mathcal{B}((\boldsymbol{w}, q), (\boldsymbol{v}, r)) := (\nabla\boldsymbol{w}, \nabla\boldsymbol{v})_\Omega - (q, \nabla\cdot\boldsymbol{v})_\Omega + (r, \nabla\cdot\boldsymbol{w})_\Omega \qquad \text{and} \qquad \mathcal{G}_{\boldsymbol{u}}(\boldsymbol{v}, r) := -((\boldsymbol{u}\cdot\nabla)\boldsymbol{u}, \boldsymbol{v})_\Omega - \nu(\nabla\boldsymbol{u}, \nabla\boldsymbol{v})_\Omega. \tag{19}$$

For the analysis, we will use the following norm

$$\|(\boldsymbol{v}, r)\|_{\mathbf{V}\times P} := |\boldsymbol{v}|_{1,\Omega} + \|r\|_{0,\Omega},$$

and if F is an linear functional operator we use the norm

$$\|F\|_{(\mathbf{V}\times P)'} := \sup_{\substack{(\boldsymbol{v},r)\in\mathbf{V}\times P\\(\boldsymbol{v},r)\neq\mathbf{0}}} \frac{|F(\boldsymbol{v},r)|}{\|(\boldsymbol{v},r)\|_{\mathbf{V}\times P}} \tag{20}$$

Note that the problem (18) is well posed thanks to the $\mathbf{V}-$ellipticity of the bilinear form $(\nabla\boldsymbol{w},\nabla\boldsymbol{v})_\Omega$, and $(q,\nabla\cdot\boldsymbol{w})_\Omega$ satisfy an inf-sup condition (cf. [7, Prop. 2.36]).

Lemma 3. *There exists a positive constant $C_{\mathcal{B}}$ such that*

$$\|\mathcal{B}\| \leq C_{\mathcal{B}}.$$

Proof. Using triangular inequality, Cauchy-Schwarz inequality, together to the inequalities $1 \leq \sqrt{d}$ and $\sqrt{a^2+b^2} \leq a+b$, with $a,b\geq 0$, we get

$$\begin{aligned}
|\mathcal{B}((\boldsymbol{w},q),(\boldsymbol{v},r))| &\leq |\boldsymbol{w}|_{1,\Omega}|\boldsymbol{v}|_{1,\Omega} + \sqrt{d}\|q\|_{0,\Omega}|\boldsymbol{v}|_{1,\Omega} + \sqrt{d}\|r\|_{0,\Omega}|\boldsymbol{w}|_{1,\Omega}\\
&\leq \sqrt{d}|\boldsymbol{w}|_{1,\Omega}|\boldsymbol{v}|_{1,\Omega} + \sqrt{d}\|q\|_{0,\Omega}|\boldsymbol{v}|_{1,\Omega} + \sqrt{d}\|r\|_{0,\Omega}|\boldsymbol{w}|_{1,\Omega}\\
&\leq \sqrt{d}(|\boldsymbol{w}|^2_{1,\Omega} + |\boldsymbol{w}|^2_{1,\Omega} + \|q\|_{0,\Omega})^{1/2}(|\boldsymbol{v}|^2_{1,\Omega} + |\boldsymbol{v}|^2_{1,\Omega} + \|r\|_{0,\Omega})^{1/2}\\
&\leq C_{\mathcal{B}}(|\boldsymbol{w}|^2_{1,\Omega} + \|q\|^2_{0,\Omega})^{1/2}(|\boldsymbol{v}|^2_{1,\Omega} + \|r\|^2_{0,\Omega})^{1/2}\\
&\leq C_{\mathcal{B}}\|(\boldsymbol{w},q)\|_{\mathbf{V}\times P}\|(\boldsymbol{v},r)\|_{\mathbf{V}\times P},
\end{aligned}$$

and the result is obtained directly, with $C_{\mathcal{B}} = 2\sqrt{d}$. ■

3.2. Discrete spaces

Let us denote by $\{\mathcal{T}_h\}$ a regular family partition of Ω composed of triangular elements K of diameter h_K. We will denote by h the mesh size, where $h = \max\{h_K : K\in\mathcal{T}_h\}$.
Now, for each h let $\mathbf{W}_h$ and P_h be finite-dimensional spaces such that:

$$\begin{aligned}
\mathbf{W}_h &:= \left\{\boldsymbol{v}_h \in [H^1(\Omega)]^d : \boldsymbol{v}_h|_K \in [\mathcal{P}_l(K)]^d \quad \forall K\in\mathcal{T}_h\right\},\\
P_h &:= \left\{q_h \in P : q_h|_K \in \mathcal{P}_k(K) \quad \forall K\in\mathcal{T}_h\right\},\\
\boldsymbol{H}_h &:= \left\{\boldsymbol{w}_h \in \boldsymbol{H} : \boldsymbol{w}_h|_K \in [\mathcal{P}_1(K)]^d \quad \forall K\in\mathcal{T}_h\right\}.
\end{aligned}$$

For our error analysis we will need to make use of some known results.

Theorem 2. *For all $\boldsymbol{w}\in[\mathcal{P}_l(K)]^d$ there holds,*

$$\|\nabla\boldsymbol{w}\|_{0,K} \leq \sqrt{\kappa_l}\frac{|\partial K|}{|K|}\|\boldsymbol{w}\|_{0,K}. \tag{21}$$

For $d=2$, it holds $\kappa_1 = 6$ and $\kappa_2 = \dfrac{45}{2}$.

Proof. See [15, Theorem 2] ■

Corollary 2. *For $d=2$ and $l=1$ there holds*

$$\|\nabla\boldsymbol{w}\|_{0,K} \leq C_I h_K^{-1}\|\boldsymbol{w}\|_{0,K}, \tag{22}$$

where $C_I = \dfrac{6\sqrt{\kappa_1}}{\sin^2(\theta)}$, being θ the minimun angle of the element K.

Proof. The proof is a direct consequence of the minimum angle condition and Theorem 2. ■

For the discrete STE we set $\mathbf{V}_h = \mathbf{W}_h \cap \mathbf{V}$ where inf-sup stable pairs of finite elements requires the use of different spaces for velocity and pressure and for this reason we take Taylor-Hood, where $l = k+1$. Otherwise, it is not possible to use conforming spaces of lowest order for the discrete velocity. Furthermore, we will consider the property of interpolation operator $\mathcal{I}_h : \mathbf{V} \cap [H^{k+1}(\Omega)]^d \to \mathbf{V}_h$:

$$|\boldsymbol{w} - \mathcal{I}_h \boldsymbol{w}|_{m,\Omega} \leq a_k\, h^{k+1-m} |\boldsymbol{w}|_{k+1,\Omega}, \qquad \forall \boldsymbol{w} \in [H^{k+1}(\Omega)]^d,\ 0 \leq m \leq k+1, \tag{23}$$

Thereby, the discrete version of the problem (18) reads as follows: *Find* $(\boldsymbol{w}_h, q_h) \in \mathbf{V}_h \times P_h$ *such that*

$$\mathcal{B}((\boldsymbol{w}_h, q_h), (\boldsymbol{v}_h, r_h)) = \mathcal{G}_{\boldsymbol{u}_h}(\boldsymbol{v}_h, r_h) \quad \forall (\boldsymbol{v}_h, r_h) \in \mathbf{V}_h \times P_h, \tag{24}$$

where the bilinear form $\mathcal{B}$ is like in the continuous case, and

$$\mathcal{G}_{\boldsymbol{u}_h}(\boldsymbol{v}_h, r_h) := -((\mathcal{L}_h \boldsymbol{u} \cdot \nabla)\mathcal{L}_h \boldsymbol{u}, \boldsymbol{v}_h)_\Omega - \nu(\nabla \mathcal{L}_h \boldsymbol{u}, \nabla \boldsymbol{v}_h)_\Omega, \tag{25}$$

with $\mathcal{L}_h : [H^2(\Omega)]^d \longrightarrow \boldsymbol{H}_h$ a Lagrange interpolant.

Lemma 4. *There exists a constant* β_1*, independent of* h*, such that*

$$\sup_{\substack{(\boldsymbol{v}_h, r_h) \in \mathbf{V}_h \times P_h \\ (\boldsymbol{v}_h, r_h) \neq \mathbf{0}}} \frac{\mathcal{B}((\boldsymbol{w}_h, q_h), (\boldsymbol{v}_h, r_h))}{\|(\boldsymbol{v}_h, r_h)\|_{\mathbf{V} \times P}} \geq \beta_1 \|(\boldsymbol{w}_h, q_h)\|_{\mathbf{V} \times P}, \qquad \forall\ (\boldsymbol{w}_h, q_h)\ \in\ \mathbf{V}_h \times P_h.$$

Proof. See equation [8, (1.39)] and [8, Corollary 4.1] ■

For the next result, we consider the pair $(\tilde{\boldsymbol{w}}_h, \tilde{q}_h) \in \mathbf{V}_h \times P_h$, such that

$$\mathcal{B}((\tilde{\boldsymbol{w}}_h, \tilde{q}_h), (\boldsymbol{v}_h, r_h)) = \mathcal{G}_{\boldsymbol{u}}(\boldsymbol{v}_h, r_h) \quad \forall (\boldsymbol{v}_h, r_h) \in \mathbf{V}_h \times P_h, \tag{26}$$

where $\mathcal{G}_{\boldsymbol{u}}(\boldsymbol{v}_h, r_h) = -((\boldsymbol{u} \cdot \nabla)\boldsymbol{u}, \boldsymbol{v}_h)_{0,\Omega} - \nu(\nabla \boldsymbol{u}, \nabla \boldsymbol{v}_h)_\Omega$ with the continuous velocity $\boldsymbol{u}$. Let us recall the following convergence result.

Lemma 5. *Let* $(\boldsymbol{w}, q)$ *and* $(\tilde{\boldsymbol{w}}_h, \tilde{q}_h)$ *solutions of* (18) *and* (26) *respectively. Assume that* $(\boldsymbol{w}, q) \in [H_0^1(\Omega) \cap H^{k+1}(\Omega)]^d \times [L_0^2(\Omega) \cap H^k(\Omega)]$*, with* $k \geq 1$*. Then, there exists* $C > 0$ *independent of* h *such that*

$$\|(\boldsymbol{w} - \tilde{\boldsymbol{w}}_h, q - \tilde{q}_h)\|_{\mathbf{V} \times P} \leq C_1 C_2 h^k \big(|\boldsymbol{w}|_{k+1,\Omega} + |q|_{k,\Omega}\big),$$

with $C_2 = 1 + \dfrac{C_{\mathcal{B}}}{\beta_1}$ *and* β_1 *being the constant given in Lemma 4.*

Proof. See [7, Lemma 2.44]

■

In order to show the convergence of q_h (Main Result I, see later Theorem 3), we set the following Lemma.

Lemma 6. *Let* $(\boldsymbol{w}_h, q_h), (\tilde{\boldsymbol{w}}_h, \tilde{q}_h) \in \mathbf{V}_h \times P_h$*, solutions of* (24) *and* (26) *respectively, and* β_1 *the constant given in Lemma 4. Then,*

$$\|(\tilde{\boldsymbol{w}}_h - \boldsymbol{w}_h, \tilde{q}_h - q_h)\|_{\mathbf{V} \times P} \leq \beta_1^{-1} \|\mathcal{G}_{\boldsymbol{u}} - \mathcal{G}_{\boldsymbol{u}_h}\|_{(\mathbf{V} \times P)'}$$

with $(\mathcal{G}_{\boldsymbol{u}} - \mathcal{G}_{\boldsymbol{u}_h})(\boldsymbol{v}_h, r_h) := -((\boldsymbol{u} \cdot \nabla)\boldsymbol{u} - (\mathcal{L}_h \boldsymbol{u} \cdot \nabla)\mathcal{L}_h \boldsymbol{u}, \boldsymbol{v}_h)_\Omega - \nu(\nabla \boldsymbol{u} - \nabla \mathcal{L}_h \boldsymbol{u}, \nabla \boldsymbol{v}_h)_\Omega$.

Proof. By Lemma 4 together with the Cauchy - Schwarz inequality, we arrive to the inequality

$$\beta_1 \|(\tilde{\boldsymbol{w}}_h - \boldsymbol{w}_h, \tilde{q}_h - q_h)\|_{\mathbf{V} \times P} \leq \sup_{\substack{(\boldsymbol{v}_h, r_h) \in \mathbf{V}_h \times P_h \\ (\boldsymbol{v}_h, r_h) \neq \mathbf{0}}} \frac{\mathcal{B}((\tilde{\boldsymbol{w}}_h - \boldsymbol{w}_h, \tilde{q}_h - q_h), (\boldsymbol{v}_h, r_h))}{\|(\boldsymbol{v}_h, r_h)\|_{\mathbf{V} \times P}}$$

$$
\begin{aligned}
&= \sup_{\substack{(\boldsymbol{v}_h, r_h)\in \mathbf{V}_h\times P_h \\ (\boldsymbol{v}_h, r_h)\neq \mathbf{0}}} \frac{\mathcal{G}_{\boldsymbol{u}}(\boldsymbol{v}_h, r_h) - \mathcal{G}_{\boldsymbol{u}_h}(\boldsymbol{v}_h, r_h)}{\|(\boldsymbol{v}_h, r_h)\|_{\mathbf{V}\times P}} \\
&= \sup_{\substack{(\boldsymbol{v}_h, r_h)\in \mathbf{V}_h\times P_h \\ (\boldsymbol{v}_h, r_h)\neq \mathbf{0}}} \frac{(\mathcal{G}_{\boldsymbol{u}} - \mathcal{G}_{\boldsymbol{u}_h})(\boldsymbol{v}_h, r_h)}{\|(\boldsymbol{v}_h, r_h)\|_{\mathbf{V}\times P}} \\
&\leq \|\mathcal{G}_{\boldsymbol{u}} - \mathcal{G}_{\boldsymbol{u}_h}\|_{(\mathbf{V}\times P)'}.
\end{aligned}
$$

■

Lemma 7. *Let $\mathcal{G}_{\boldsymbol{u}}$ and $\mathcal{G}_{\boldsymbol{u}_h}$ be as in* (19) *and* (25) *respectively and denote by $(\mathbf{V}\times P)'$ the dual space of the product space $\mathbf{V}\times P$. In addition, we assume that $\boldsymbol{u}\in[H^2(\Omega)]^d$. Then*

$$
\|\mathcal{G}_{\boldsymbol{u}} - \mathcal{G}_{\boldsymbol{u}_h}\|_{(\mathbf{V}\times P)'} \leq h|\boldsymbol{u}|_{2,\Omega}\Big[C_p\,\tilde{C}(a_1 + a_2\,C_I)\|\boldsymbol{u}\|_{2,\Omega} + \nu\,a_1\Big].
$$

Proof.

$$
\|\mathcal{G}_{\boldsymbol{u}}(\boldsymbol{v}_h, r_h) - \mathcal{G}_{\boldsymbol{u}_h}(\boldsymbol{v}_h, r_h)\|_{0,\Omega} \leq \|(\boldsymbol{u}\cdot\nabla)\boldsymbol{u} - (\mathcal{L}_h\boldsymbol{u}\cdot\nabla)\mathcal{L}_h\boldsymbol{u})\|_{0,\Omega}\|\boldsymbol{v}_h\|_{0,\Omega} + \nu\|\nabla\boldsymbol{u} - \nabla\mathcal{L}_h\boldsymbol{u}\|_{0,\Omega}\|\nabla\boldsymbol{v}_h\|_{0,\Omega}.
$$

For the first term of the right-hand side, we use Lemma 1.
For the second term of the right-hand-side, we have from the interpolation bounds:

$$
\|\nabla(\boldsymbol{u} - \mathcal{L}_h\boldsymbol{u})\|_{0,\Omega} \leq a_1 h|\boldsymbol{u}|_{2,\Omega}.
$$

Finally, using the above inequalities and Poincaré inequality we get

$$
\begin{aligned}
\|(\mathcal{G}_{\boldsymbol{u}} - \mathcal{G}_{\boldsymbol{u}_h})(\boldsymbol{v}_h, r_h)\|_{0,\Omega} &\leq h|\boldsymbol{u}|_{2,\Omega}\Big[C_p\,\tilde{C}\,(a_1 + a_2\,C_I)\|\boldsymbol{u}\|_{2,\Omega} + \nu\,a_1\Big]|\boldsymbol{v}_h|_{1,\Omega} \\
&\leq h|\boldsymbol{u}|_{2,\Omega}\Big[C_p\,\tilde{C}\,(a_1 + a_2\,C_I)\|\boldsymbol{u}\|_{2,\Omega} + \nu\,a_1\Big]\|(\boldsymbol{v}_h, r_h)\|_{\mathbf{V}\times P},
\end{aligned}
$$

where C_p is the Poincaré constant. Thereby, we arrive straight to the result of the lemma.¸

■

Finally, we can derive the first main convergence result.

Theorem 3 (Main Result II). *Assume that $(\boldsymbol{w}, q)\in[H_0^1(\Omega)\cap H^{k+1}(\Omega)]^d\times[L_0^2(\Omega)\cap H^k(\Omega)]$ and $\boldsymbol{u}\in[H^2(\Omega)]^d$. Then,*

$$
|\boldsymbol{w} - \boldsymbol{w}_h|_{1,\Omega} + \|q - q_h\|_{0,\Omega} \leq C_1C_2h^k\big(|\boldsymbol{w}|_{k+1,\Omega} + |q|_{k,\Omega}\big) + \beta_1^{-1}h|\boldsymbol{u}|_{2,\Omega}\Big(\rho\,C_p\,\tilde{C}\,(a_1 + a_2\,C_I)\|\boldsymbol{u}\|_{2,\Omega} + \mu\,a_1\Big).
$$

Proof. The proof follows from Lemmas 5, 6, and 7. ■

3.4. Stabilized PSPG discretization

Let us consider again the Stokes problem given as in (17) and its respective variational formulation (18). We will now analyze the PSPG Stabilization [10] with the end of comparing the error of convergence between the pressure obtained with both schemes.
We want to use spaces of finite element of order k for the velocity and the pressure, i.e., $k = l$, by means of the following stabilized formulation.

$$
\mathcal{B}^s((\boldsymbol{w}_h, q_h)(\boldsymbol{v}_h, r_h)) = \mathcal{G}^s_{\boldsymbol{u}_h}(\boldsymbol{v}_h, r_h) \tag{27}
$$

where

$$\mathcal{B}^s((\boldsymbol{w}_h,q_h)(\boldsymbol{v}_h,r_h)) := \mathcal{B}((\boldsymbol{w}_h,q_h)(\boldsymbol{v}_h,r_h)) + \sum_{K\in\mathcal{T}_h} \delta\, h_K^2(\nabla q_h,\nabla r_h)_K$$

$$\mathcal{G}^s_{\boldsymbol{u}_h}(\boldsymbol{v}_h,r_h) := \mathcal{G}_{\boldsymbol{u}_h}(\boldsymbol{v}_h,r_h) + \sum_{K\in\mathcal{T}_h} \delta\, h_K^2(-\boldsymbol{f}_{\boldsymbol{u}_h},\nabla r_h)_K$$

with $\mathcal{B}((\cdot,\cdot),(\cdot,\cdot))$ and $\mathcal{G}_{\boldsymbol{u}_h}(\cdot,\cdot)$ defined as in (25), and

$$\boldsymbol{f}_{\boldsymbol{u}_h} := (\mathcal{L}_h\boldsymbol{u}\cdot\nabla)\mathcal{L}_h\boldsymbol{u}. \tag{28}$$

Remark 2. *Note that the term $\Delta\boldsymbol{w}_h$ is not included in the stabilization. This is possible to do while keeping strong consistency since $\boldsymbol{w}=\boldsymbol{0}$. Our choice allows also to avoid conditional well-posedness of the discrete solution as in standard PSPG stabilized formulations.*

Let us define the mesh-dependent norm on the product space $\mathbf{V}\times P$

$$\|(\boldsymbol{v},r)\|_h^2 := \mathcal{B}^s((\boldsymbol{v},r),(\boldsymbol{v},r)) = \|\nabla\boldsymbol{v}\|_{0,\Omega}^2 + \sum_{K\in\mathcal{T}_h}\delta h_K^2\|\nabla r\|_{0,K}^2. \tag{29}$$

Remark 3. *It is possible to prove that $\|(\boldsymbol{v}_h,r_h)\|_h \preceq \|(\boldsymbol{v}_h,r_h)\|_{\mathbf{V}\times P}$ for all $(\boldsymbol{v}_h,r_h)\in\mathbf{V}_h\times P_h$. Indeed, applying the inequality* (22) *and the previous assumptions we get*

$$\|(\boldsymbol{v}_h,r_h)\|_h^2 := \|\nabla\boldsymbol{v}_h\|_{0,\Omega}^2 + \sum_{K\in\mathcal{T}_h}\delta h_K^2\|\nabla r_h\|_{0,K}^2 \le \|\nabla\boldsymbol{v}_h\|_{0,\Omega}^2 + \delta C_I^2\|r_h\|_{0,\Omega}^2 \le \max\left\{1,\delta C_I^2\right\}(\|\nabla\boldsymbol{v}_h\|_{0,\Omega}^2 + \|r_h\|_{0,\Omega}^2),$$

and then,

$$\|(\boldsymbol{v}_h,r_h)\|_h \le C_{eq}\|(\boldsymbol{v}_h,r_h)\|_{\mathbf{V}\times P}, \tag{30}$$

where

$$C_{eq} = \left[\max\left\{1,\delta C_I^2\right\}\right]^{1/2}$$

Lemma 8.

$$\|\mathcal{B}^s\| \le C_{\mathcal{B}^s} = \max\left\{C_{\mathcal{B}},\sqrt{\delta}C_{eq}\,C_I\right\} \tag{31}$$

Proof. Using the inequalities (22) and (30), Theorem 3 and Cauchy-Schwarz inequality we obtain that

$$\begin{aligned}
|\mathcal{B}^s((\boldsymbol{w}_h,q_h),(\boldsymbol{v}_h,r_h))| &\le \|\mathcal{B}\|\|(\boldsymbol{w}_h,q_h)\|_{\mathbf{V}\times P}\|(\boldsymbol{v}_h,r_h)\|_{\mathbf{V}\times P} + \sum_{K\in\mathcal{T}_h}\delta h_K^2\|\nabla q_h\|_{0,K}\|\nabla r_h\|_{0,K}\\
&\le C_{\mathcal{B}}\|(\boldsymbol{w}_h,q_h)\|_{\mathbf{V}\times P}\|(\boldsymbol{v}_h,r_h)\|_{\mathbf{V}\times P} + \left(\sum_{K\in\mathcal{T}_h}\delta h_K^2\|\nabla q_h\|_{0,K}^2\right)^{1/2}\left(\sum_{K\in\mathcal{T}_h}\delta h_K^2\|\nabla r_h\|_{0,K}^2\right)^{1/2}\\
&\le C_{\mathcal{B}}\|(\boldsymbol{w}_h,q_h)\|_{\mathbf{V}\times P}\|(\boldsymbol{v}_h,r_h)\|_{\mathbf{V}\times P} + \left(\sum_{K\in\mathcal{T}_h}\delta C_I^2\|q_h\|_{0,K}^2\right)^{1/2}\|(\boldsymbol{v}_h,r_h)\|_h\\
&\le C_{\mathcal{B}^s}\|(\boldsymbol{w}_h,q_h)\|_{\mathbf{V}\times P}\|(\boldsymbol{v}_h,r_h)\|_{\mathbf{V}\times P},
\end{aligned}$$

and then the result follows. ∎

In the next lemmas we will consider the pair $(\tilde{\boldsymbol{w}}_h,\tilde{q}_h)\in\mathbf{V}_h\times P_h$ which are solution of the equation

$$\mathcal{B}^s((\boldsymbol{w}_h,q_h)(\boldsymbol{v}_h,r_h)) = \mathcal{G}^s_{\boldsymbol{u}}(\boldsymbol{v}_h,r_h), \qquad \forall\ (\boldsymbol{v}_h,r_h)\in\mathbf{V}_h\times P_h \tag{32}$$

where

$$\mathcal{G}^s_{\boldsymbol{u}}(\boldsymbol{v}_h,r_h) := \mathcal{G}_{\boldsymbol{u}}(\boldsymbol{v}_h,r_h) + \sum_{K\in\mathcal{T}_h}\delta\, h_K^2(\boldsymbol{f}_{\boldsymbol{u}},\nabla r_h)_K.$$

We highlight that the solvability of the problem (32) has been guaranteed in [10].

Lemma 9. *Let $(\boldsymbol{w}, q)$ and $(\tilde{\boldsymbol{w}}_h, \tilde{q}_h)$ solutions of (18) and (32) respectively. Assume that $(\boldsymbol{w}, q) \in [H_0^1(\Omega) \cap H^{k+1}(\Omega)]^d \times [L_0^2(\Omega) \cap H^k(\Omega)]$. Then, there is $C > 0$ independent of h such that*

$$|\boldsymbol{w} - \tilde{\boldsymbol{w}}_h|_{1,\Omega} + \|q - \tilde{q}_h\|_{0,\Omega} \leq C_1\, C_3\, h^k \big(|\boldsymbol{w}|_{k+1,\Omega} + |q|_{k,\Omega}\big)$$

with $C_3 = 1 + \|\mathcal{B}^s\|$.

Proof.
We note that $(\boldsymbol{w}, q)$ and $(\tilde{\boldsymbol{w}}_h, \tilde{q}_h)$ satisfy the orthogonality property

$$\mathcal{B}^s((\boldsymbol{w} - \tilde{\boldsymbol{w}}_h, q - \tilde{q}_h), (\boldsymbol{v}_h, r_h)) = 0 \qquad \forall (\boldsymbol{v}_h, r_h) \in \mathbf{V}_h \times P_h.$$

Indeed, thanks to the consistency of bilinear form $\mathcal{B}$ we get

$$\begin{aligned}
\mathcal{B}^s((\boldsymbol{w} - \tilde{\boldsymbol{w}}_h, q - \tilde{q}_h), (\boldsymbol{v}_h, r_h)) &= \mathcal{B}((\boldsymbol{w} - \tilde{\boldsymbol{w}}_h, q - \tilde{q}_h), (\boldsymbol{v}_h, r_h)) + \sum_{K \in \mathcal{T}_h} \delta h_K^2 (\nabla q, \nabla r_h)_K \\
&\quad - \sum_{K \in \mathcal{T}_h} \delta h_K^2 (\nabla \tilde{q}_h, \nabla r_h)_K \\
&= \sum_{K \in \mathcal{T}_h} \delta h_K^2 (\boldsymbol{f}_{\boldsymbol{u}}, \nabla r_h)_K - \sum_{K \in \mathcal{T}_h} \delta h_K^2 (\boldsymbol{f}_{\boldsymbol{u}}, \nabla r_h)_K \\
&= 0.
\end{aligned}$$

By the triangle inequality we can get,

$$\begin{aligned}
\|(\boldsymbol{w} - \tilde{\boldsymbol{w}}_h, q - \tilde{q}_h)\|_{\mathbf{V} \times P} &= |\boldsymbol{w} - \mathcal{I}_h \boldsymbol{w} + \mathcal{I}_h \boldsymbol{w} - \boldsymbol{w}_h|_{1,\Omega} + \|q - \mathcal{J}_h q + \mathcal{J}_h q - q_h\|_{0,\Omega} \\
&\leq \|(\boldsymbol{w} - \mathcal{I}_h \boldsymbol{w}, q - \mathcal{J}_h q)\|_{\mathbf{V} \times P} + \|(\tilde{\boldsymbol{w}}_h - \mathcal{I}_h \boldsymbol{w}, \tilde{q}_h - \mathcal{J}_h q)\|_{\mathbf{V} \times P}. \qquad (33)
\end{aligned}$$

For the second term of the right-hand side, we must consider the result earned in [10] from where we get

$$\begin{aligned}
\|(\tilde{\boldsymbol{w}}_h - \mathcal{I}_h \boldsymbol{w}, \tilde{q}_h - \mathcal{J}_h q)\|_{\mathbf{V} \times P} &\leq \sup_{\substack{(\boldsymbol{v}_h, r_h) \in \mathbf{V}_h \times P_h \\ (\boldsymbol{v}_h, r_h) \neq \mathbf{0}}} \frac{\mathcal{B}^s((\tilde{\boldsymbol{w}}_h - \mathcal{I}_h \boldsymbol{w}, \tilde{q}_h - \mathcal{J}_h q), (\boldsymbol{v}_h, r_h))}{\|(\boldsymbol{v}_h, r_h)\|_h} \\
&= \sup_{\substack{(\boldsymbol{v}_h, r_h) \in \mathbf{V}_h \times P_h \\ (\boldsymbol{v}_h, r_h) \neq \mathbf{0}}} \frac{\mathcal{B}^s((\boldsymbol{w} - \mathcal{I}_h \boldsymbol{w}, q - \mathcal{J}_h q), (\boldsymbol{v}_h, r_h))}{\|(\boldsymbol{v}_h, r_h)\|_h} \\
&\leq \|\mathcal{B}^s\| \|(\boldsymbol{w} - \mathcal{I}_h \boldsymbol{w}, q - \mathcal{J}_h q)\|_{\mathbf{V} \times P},
\end{aligned}$$

and so, from this inequality and (33) we obtain

$$\|(\boldsymbol{w} - \tilde{\boldsymbol{w}}_h, q - \tilde{q}_h)\|_{\mathbf{V} \times P} \leq \big(1 + \|\mathcal{B}^s\|\big) \|(\boldsymbol{w} - \mathcal{I}_h \boldsymbol{w}, q - \mathcal{J}_h q)\|_{\mathbf{V} \times P}$$

and thereby we arrive to

$$|\boldsymbol{w} - \tilde{\boldsymbol{w}}_h|_{1,\Omega} + \|q - \tilde{q}_h\|_{0,\Omega} \leq C_1 C_3 h^k \big(|\boldsymbol{w}|_{k+1,\Omega} + |q|_{k,\Omega}\big),$$

. ■

Lemma 10. *Let $(\tilde{\boldsymbol{w}}_h, \tilde{q}_h)$ and $(\boldsymbol{w}_h, q_h)$ be solutions of (32) and (27), respectively. Additionally, we assume that $\boldsymbol{u} \in [H^2(\Omega)]^d$. Then, the following bound is satisfied:*

$$\|(\tilde{\boldsymbol{w}}_h - \boldsymbol{w}_h, \tilde{q}_h - q_h)\|_h \leq \|\mathcal{G}_{\boldsymbol{u}} - \mathcal{G}_{\boldsymbol{u}_h}\|_{(\mathbf{V} \times P)'} + \sqrt{\delta} h^2 T(a_1, a_2, \boldsymbol{u}, h) |\boldsymbol{u}|_{2,\Omega} + \sqrt{\delta} \nu h \|\Delta \boldsymbol{u}\|_{0,\Omega},$$

Proof. Let $\boldsymbol{e}_h^{\boldsymbol{w}} := \tilde{\boldsymbol{w}}_h - \boldsymbol{w}_h$ and $e_h^q := \tilde{q}_h - q_h$. Then, thanks to the stability of $\mathcal{B}^s$ given in (29) we have

$$\begin{aligned}
\|(\boldsymbol{e}_h^{\boldsymbol{w}}, e_h^q)\|_h = \frac{\mathcal{B}^s((\boldsymbol{e}_h^{\boldsymbol{w}}, e_h^q)(\boldsymbol{e}_h^{\boldsymbol{w}}, e_h^q))}{\|(\boldsymbol{e}_h^{\boldsymbol{w}}, e_h^q)\|_h} &\leq \sup_{\substack{(\boldsymbol{v}_h, r_h)\in \mathbf{V}_h\times P_h \\ (\boldsymbol{v}_h, r_h)\neq \mathbf{0}}} \frac{\mathcal{B}^s((\boldsymbol{e}_h^{\boldsymbol{w}}, e_h^q)(\boldsymbol{v}_h, q_h))}{\|(\boldsymbol{v}_h, q_h)\|_h} \\
&= \sup_{\substack{(\boldsymbol{v}_h, r_h)\in \mathbf{V}_h\times P_h \\ (\boldsymbol{v}_h, r_h)\neq \mathbf{0}}} \frac{\mathcal{G}_{\boldsymbol{u}}^s(\boldsymbol{v}_h, r_h) - \mathcal{G}_{\boldsymbol{u}_h}^s(\boldsymbol{v}_h, r_h)}{\|(\boldsymbol{v}_h, q_h)\|_h} \\
&= \sup_{\substack{(\boldsymbol{v}_h, r_h)\in \mathbf{V}_h\times P_h \\ (\boldsymbol{v}_h, r_h)\neq \mathbf{0}}} \frac{\mathcal{G}_{\boldsymbol{u}}(\boldsymbol{v}_h, r_h) - \mathcal{G}_{\boldsymbol{u}_h}(\boldsymbol{v}_h, r_h) - \sum_{K\in\mathcal{T}_h} \delta h_K^2(\boldsymbol{f}_{\boldsymbol{u}} - \boldsymbol{f}_{\boldsymbol{u}_h}, \nabla r_h)_K}{\|(\boldsymbol{v}_h, q_h)\|_h}
\end{aligned}$$

We take the term within sum, making use of the Cauchy-Schwarz inequality and proceeding similarly as in (10), we obtain

$$\begin{aligned}
-\sum_{K\in\mathcal{T}_h} \delta h_K^2(\boldsymbol{f}_{\boldsymbol{u}} - \boldsymbol{f}_{\boldsymbol{u}_h}, \nabla r_h)_K &= \sum_{K\in\mathcal{T}_h} \delta h_K^2((\boldsymbol{u}\cdot\nabla)\boldsymbol{u} - (\mathcal{L}_h\boldsymbol{u}\cdot\nabla)\mathcal{L}_h\boldsymbol{u}, \nabla r_h)_K \\
&\quad - \nu \sum_{K\in\mathcal{T}_h} \delta h_K^2(\Delta\boldsymbol{u}, \nabla r_h)_K \\
&\leq \sum_{K\in\mathcal{T}_h} \delta h_K^2 \|(\boldsymbol{u}\cdot\nabla)\boldsymbol{u} - (\mathcal{L}_h\boldsymbol{u}\cdot\nabla)\mathcal{L}_h\boldsymbol{u}\|_{0,\Omega}\|\nabla r_h\|_{0,K} \\
&\quad + \nu \sum_{K\in\mathcal{T}_h} \delta h_K^2 \|\Delta\boldsymbol{u}\|_{0,K}\|\nabla r_h\|_{0,K} \\
&\leq \Big(\sum_{K\in\mathcal{T}_h} \delta h_K^2 \|(\boldsymbol{u}\cdot\nabla)\boldsymbol{u} - (\mathcal{L}_h\boldsymbol{u}\cdot\nabla)\mathcal{L}_h\boldsymbol{u}\|_{0,K}^2\Big)^{1/2}\Big(\sum_{K\in\mathcal{T}_h} \delta h_K^2 \|\nabla r_h\|_{0,K}^2\Big)^{1/2} \\
&\quad + \nu\Big(\sum_{K\in\mathcal{T}_h} \delta h_K^2 \|\Delta\boldsymbol{u}\|_{0,K}^2\Big)^{1/2}\Big(\sum_{K\in\mathcal{T}_h} \delta h_K^2 \|\nabla r_h\|_{0,K}^2\Big)^{1/2} \\
&\leq \sqrt{\delta}h^2\tilde{C}(a_1 + a_2C_I)|\boldsymbol{u}|_{2,\Omega}\|\boldsymbol{u}\|_{2,\Omega}\|(\boldsymbol{v}_h, r_h)\|_h \\
&\quad + \nu\sqrt{\delta}\Big(\sum_{K\in\mathcal{T}_h} h_K^2 \|\Delta\boldsymbol{u}\|_{0,K}^2\Big)^{1/2}\|(\boldsymbol{v}_h, r_h)\|_h \\
&\leq \sqrt{\delta}h^2\tilde{C}(a_1 + a_2C_I)|\boldsymbol{u}|_{2,\Omega}\|\boldsymbol{u}\|_{2,\Omega}\|(\boldsymbol{v}_h, r_h)\|_h \\
&\quad + \nu\sqrt{\delta}h\|\Delta\boldsymbol{u}\|_{0,\Omega}\|(\boldsymbol{v}_h, r_h)\|_h.
\end{aligned}$$

■

As a main result of this section, by employing the approximation properties and a priori estimates, we obtain the next result.

Theorem 4 (Main Result III). *Assume that the hypothesis of Theorem 3 hold. Then,*

$$\begin{aligned}
|\boldsymbol{w} - \boldsymbol{w}_h|_{1,\Omega} + \|q - q_h\|_{0,\Omega} \leq & C_1C_3h^k\big(|\boldsymbol{w}|_{k+1,\Omega} + |q|_{k,\Omega}\big) + \nu\sqrt{\delta}h\|\Delta\boldsymbol{u}\|_{0,\Omega} \\
& + h|\boldsymbol{u}|_{2,\Omega}\Big[C_p\,\tilde{C}\,(a_1 + a_2\,C_I)\|\boldsymbol{u}\|_{2,\Omega} + \nu\,a_1 + \sqrt{\delta}hC_p\,\tilde{C}\,(a_1 + a_2\,C_I)\|\boldsymbol{u}\|_{2,\Omega}\Big].
\end{aligned}$$

Proof. The proof follows from combining the results of Lemmas 7, 9 and 10. ■

4. Numerical results for the convergence analysis

In this section we present some numerical examples to illustrate the theoretical results previously described. The legends in the plots follow the notation:

- $e_1(q)$: Pressure error in L^2-norm with $\mathcal{P}_1$
- $e_2(q)$: Pressure error in L^2-norm with $\mathcal{P}_2$,

with

$$e_i(q) := \frac{\|q - q_h\|_{0,\Omega}}{\|q\|_{0,\Omega}}.$$

In addition, for Modified-PPE and Standard-PPE we will use the legend PPEvisc and PPE respectively. For the STE computed using Taylor Hood spaces and PSPS we will use the legend STE (TH) and STE (PSPG) respectively.
Every numerical routine has been sorted out using the open-source finite element libraries FEniCS [1].

Example 1. *For the first example, we consider the exact solution of the two dimensional Kovasznay flow*

$$\boldsymbol{u}(x,y) = \begin{pmatrix} 1 - e^{\lambda x}\cos(2\pi y) \\ \frac{\lambda}{2\pi} e^{\lambda x}\sin(2\pi y) \end{pmatrix}, \quad p(x,y) = \frac{1}{2}e^{\lambda x} - (e^{3\lambda} - e^{-\lambda}),$$

where $\Omega = \left(-\frac{1}{2}, \frac{3}{2}\right) \times \left(0, 2\right)$ *and the parameter* λ *is given by* $\lambda = \frac{1}{2\nu} - \sqrt{\frac{1}{4\nu^2} + 4\pi^2}$. *For this ilustration we have taken the Reynold number as in [17] which is given by* $Re = \frac{1}{\nu}$.

The convergence results for Example are shown in Figure 2 and examples of pressure and velocity fields in Figures 3–6.
First, it can be appreciated the lack of convergence of the PPE, while adding the viscous terms recovers it. Also, the STE appears to be more accurate than the PPE(visc) and it seems not to profit from the increase of polynomial order. Moreover, the STE-PSPG appears to deliver more accurate results than the STE-TH. Finally, it is worth to say that the sensitivity of all methods with respect to the polynomial order decreases when increasing the Reynolds number.

Example 2. *Next we turn to the testing the scheme, where the computational domain is the rectangle* $\Omega = [0,1]^2$ *and we consider the exact solution of the Navier-Stokes equation given by*

$$u(x,y) = (\frac{\nu}{4}e^x \sin(\nu y), \frac{1}{4}e^x \cos(\nu y)) \quad \textit{and} \quad p(x,y) = -\frac{\nu}{2}e^{2x} + \frac{\nu}{4}(e^2 - 1) \tag{34}$$

The convergence results for Example are shown in Figure 7 and the examples of pressure and velocity fields in Figures 8–11. Here, the same remarks given about the results in Example 4 apply, except that for higher Reynolds number the STE methods appear to keep the sensitivity (though worsening) when increasing the polynomial order.

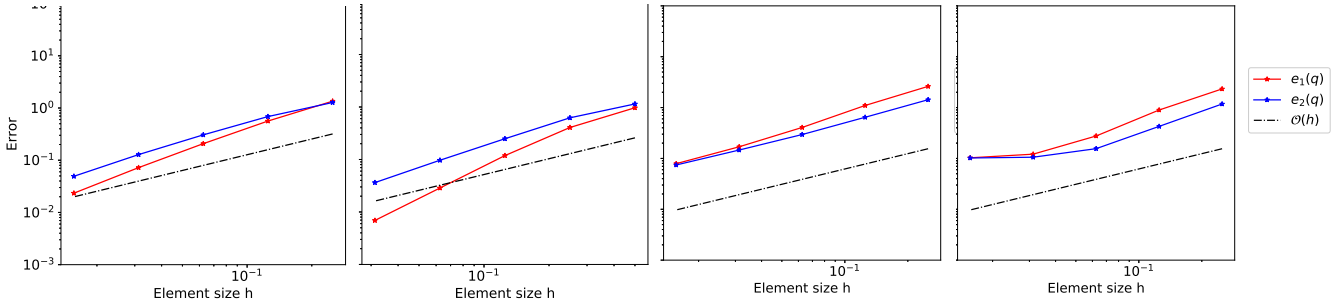

$\nu = 1$ - STE (TH) $\nu = 1$ - STE (PSPG) $\nu = 1$ - PPEvisc $\nu = 1$ - PPE

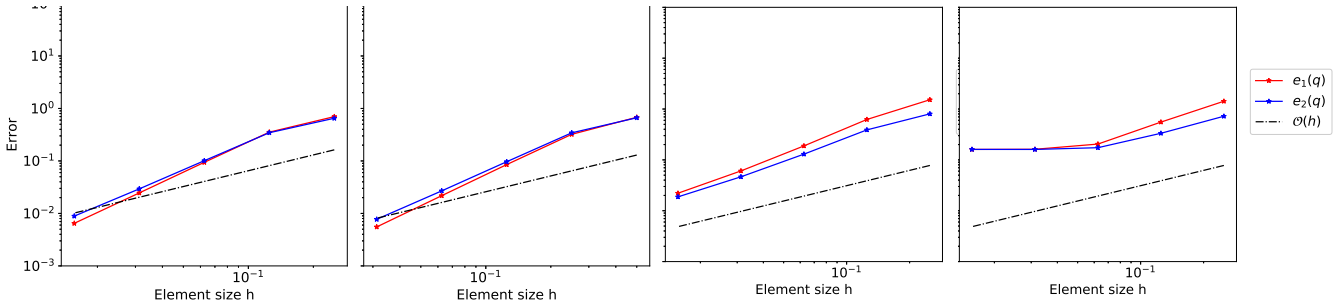

$\nu = 0.1$ - STE (TH) $\nu = 0.1$ - STE (PSPG) $\nu = 0.1$ - PPEvisc $\nu = 0.1$ - PPE

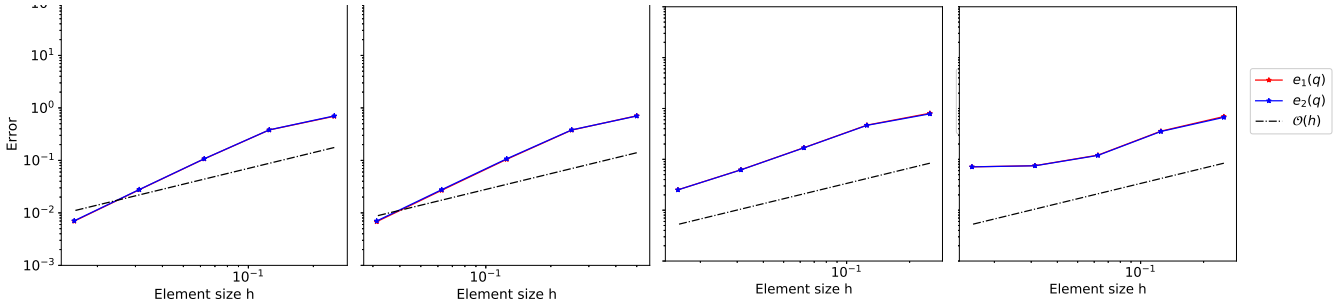

$\nu = 0.01$ - STE (TH) $\nu = 0.01$ - STE (PSPG) $\nu = 0.01$ - PPEvisc $\nu = 0.01$ - PPE

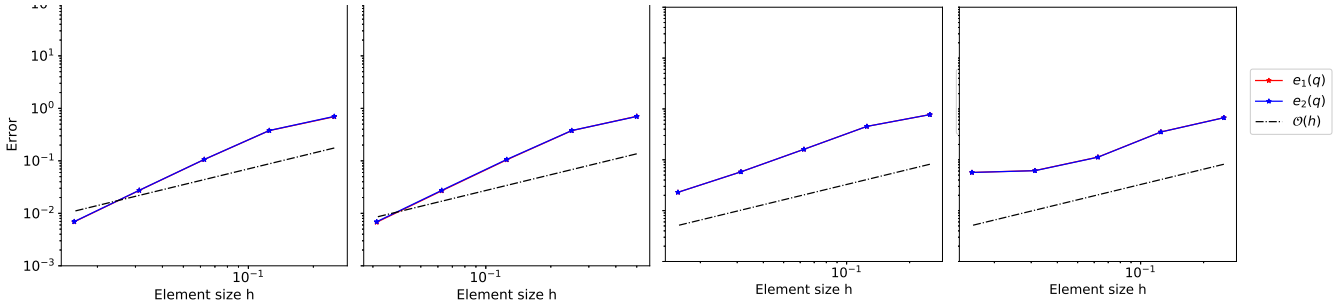

$\nu = 0.001$ - STE (TH) $\nu = 0.001$ - STE (PSPG) $\nu = 0.001$ - PPEvisc $\nu = 0.001$ - PPE

Figure 2: Pressure error curves and bounds for viscosities values $1, 10^{-1}, 10^{-2}$ and 10^{-3} of Example 1 (Kovaznay flow).

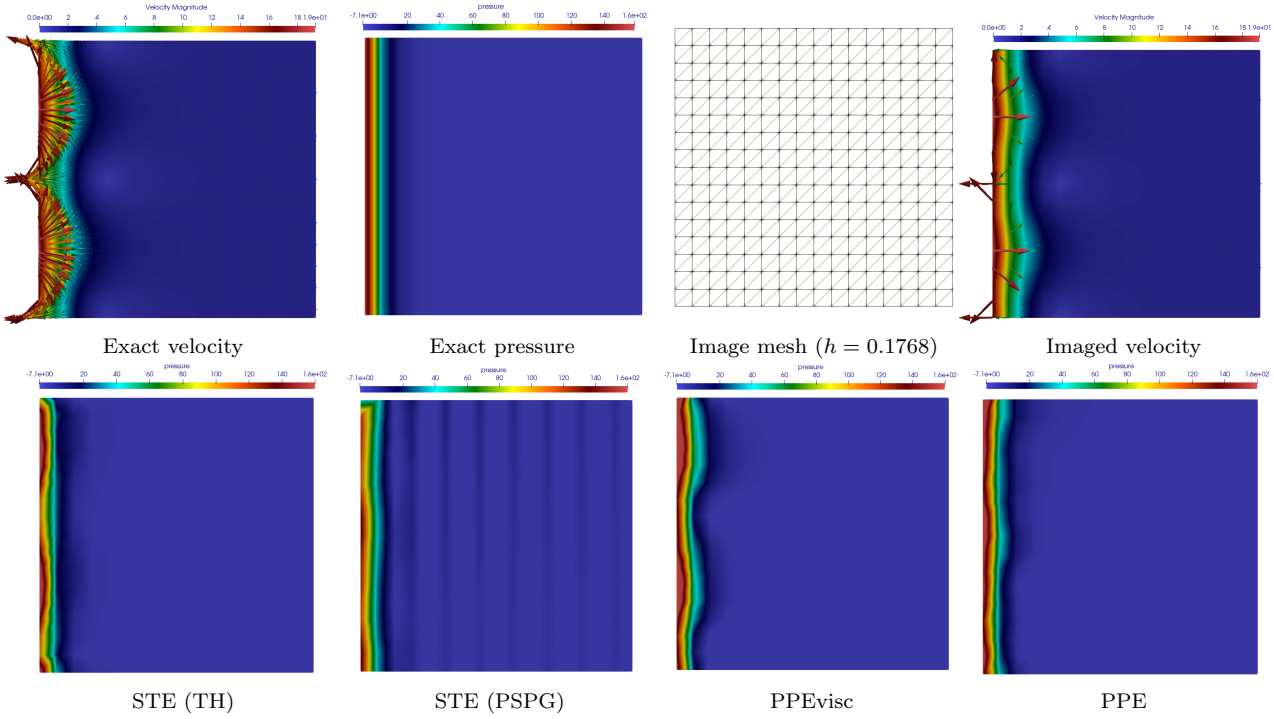

Figure 3: $\mathcal{P}_1$-interpolated reference velocity and pressure fields (top) and reconstructed pressure fields with order $k = 1$ (bottom) for $\nu = 1$ in Example 4 (Kovaznay flow).

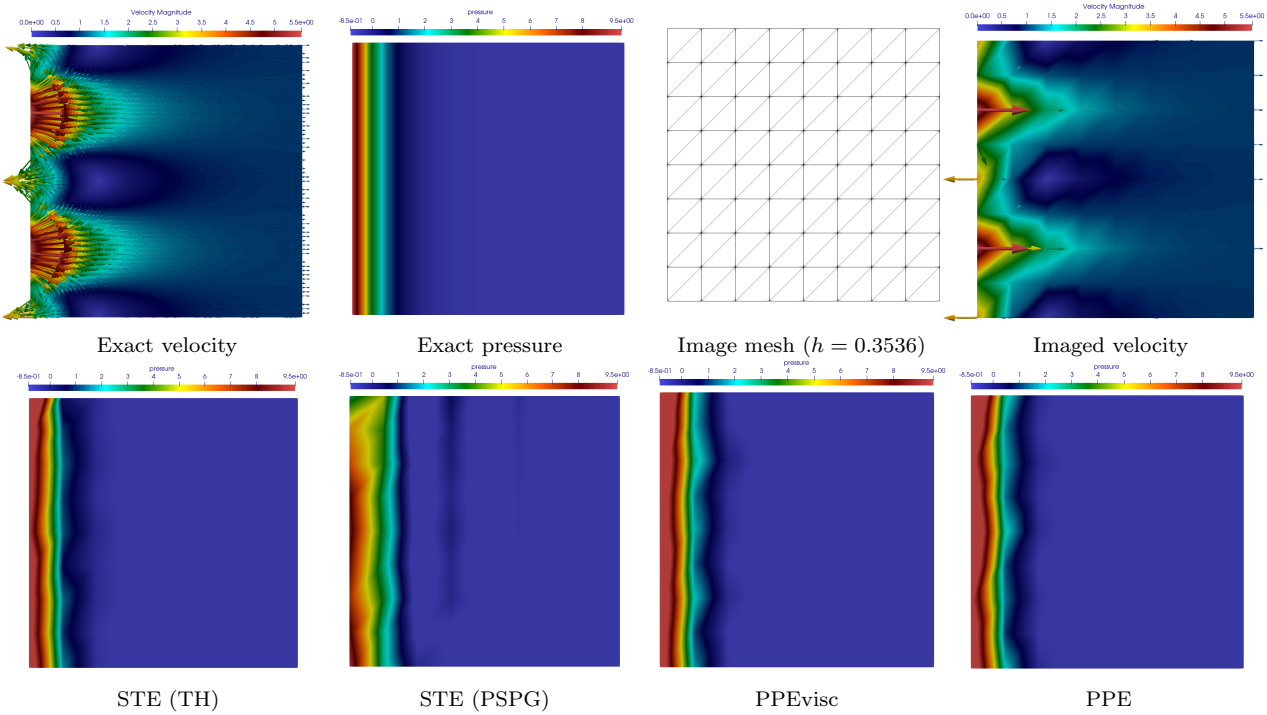

Figure 4: $\mathcal{P}_1$-interpolated reference velocity and pressure fields (top) and reconstructed pressure fields with order $k = 1$ (bottom) for $\nu = 0.1$ in Example 4 (Kovaznay flow).

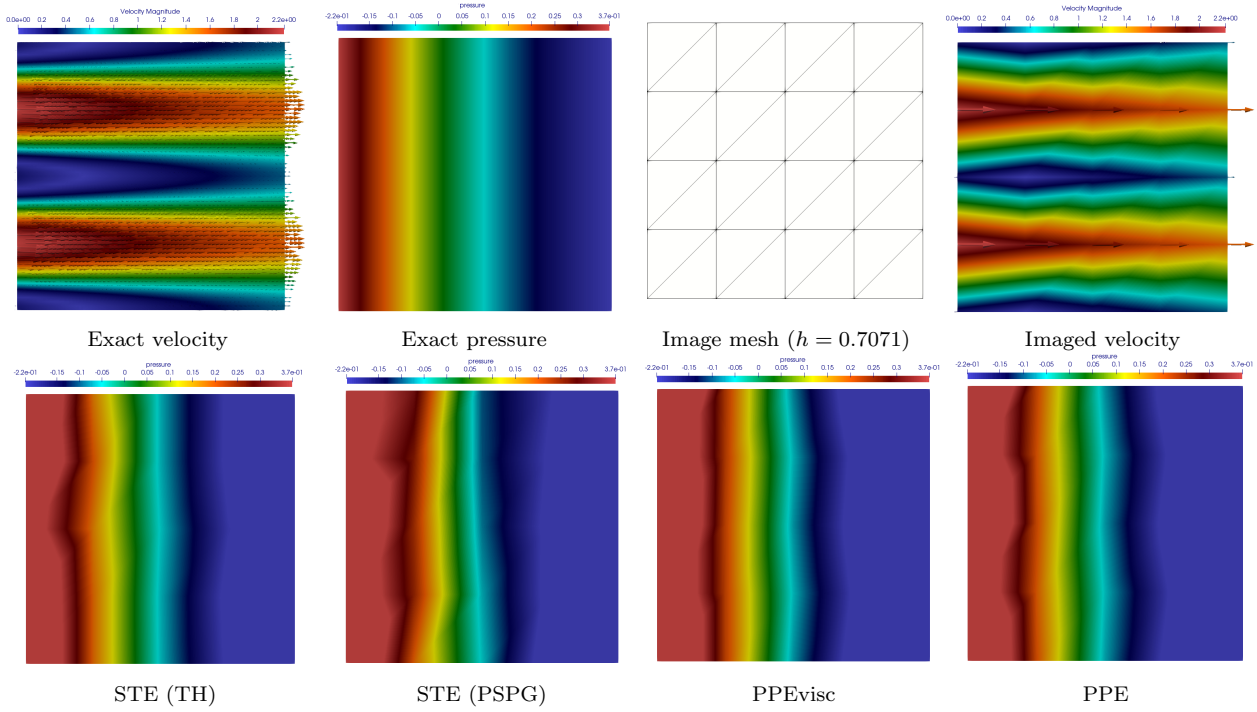

Figure 5: $\mathcal{P}_1$-interpolated reference velocity and pressure fields (top) and reconstructed pressure fields with order $k = 1$ (bottom) for $\nu = 0.01$ in Example 4 (Kovaznay flow).

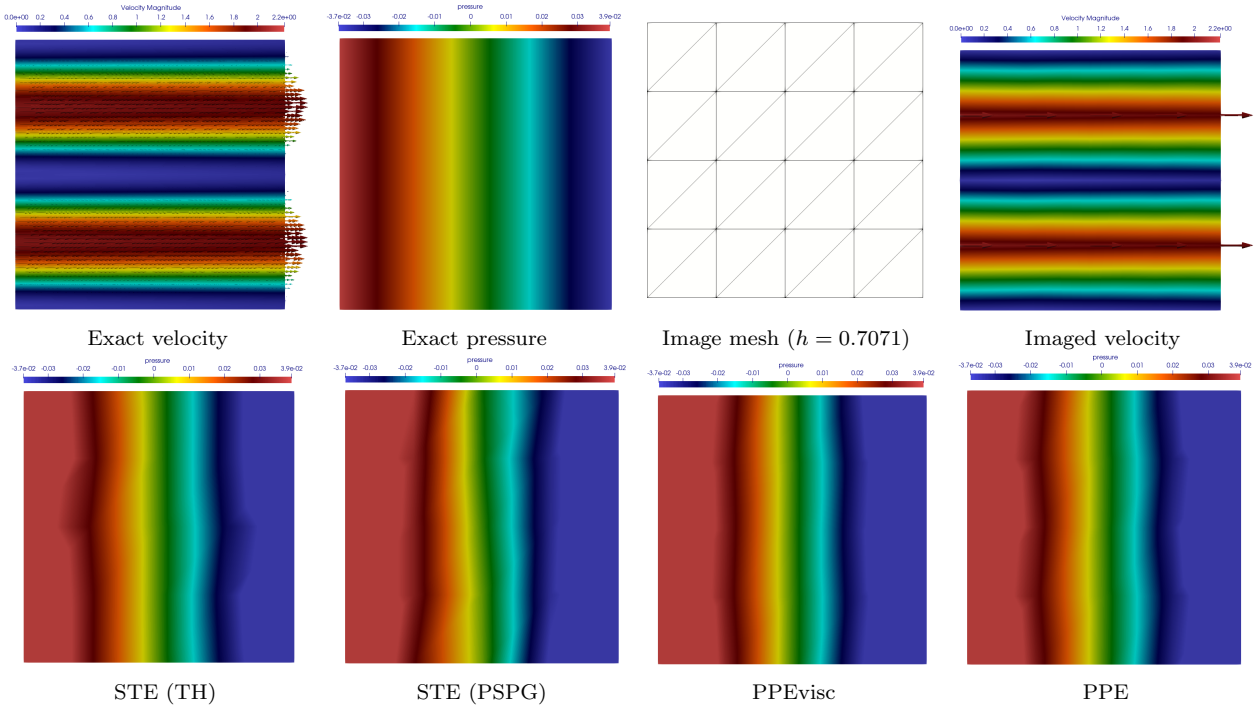

Figure 6: $\mathcal{P}_1$-interpolated reference velocity and pressure fields (top) and reconstructed pressure fields with order $k = 1$ (bottom) for $\nu = 0.001$ in Example 4 (Kovaznay flow).

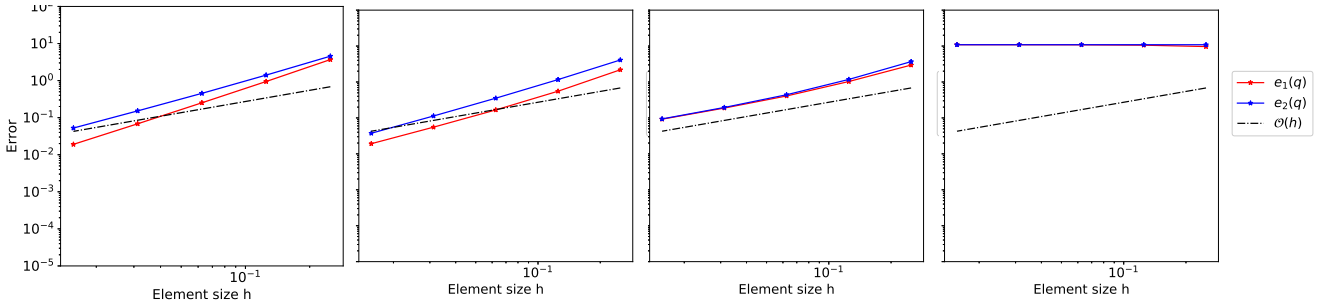

$\nu = 2\pi$ - STE (TH) $\nu = 2\pi$ - STE (PSPG) $\nu = 2\pi$ - PPEvisc $\nu = 2\pi$ - PPE

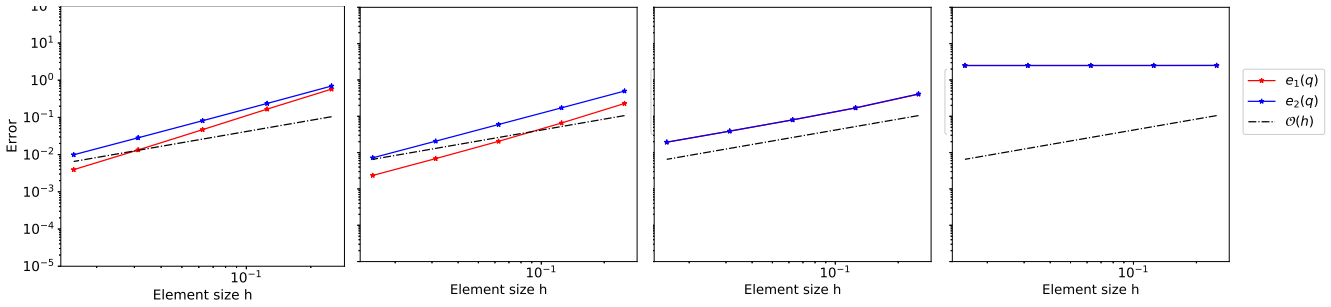

$\nu = \pi$ - STE (TH) $\nu = \pi$ - STE (PSPG) $\nu = \pi$ - PPEvisc $\nu = \pi$ - PPE

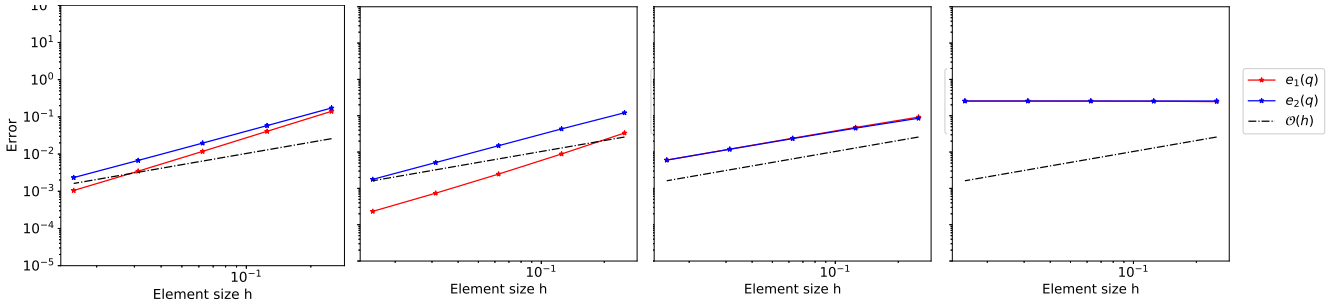

$\nu = \pi/2$ - STE (TH) $\nu = \pi/2$ - STE (PSPG) $\nu = \pi/2$ - PPEvisc $\nu = \pi/2$ - PPE

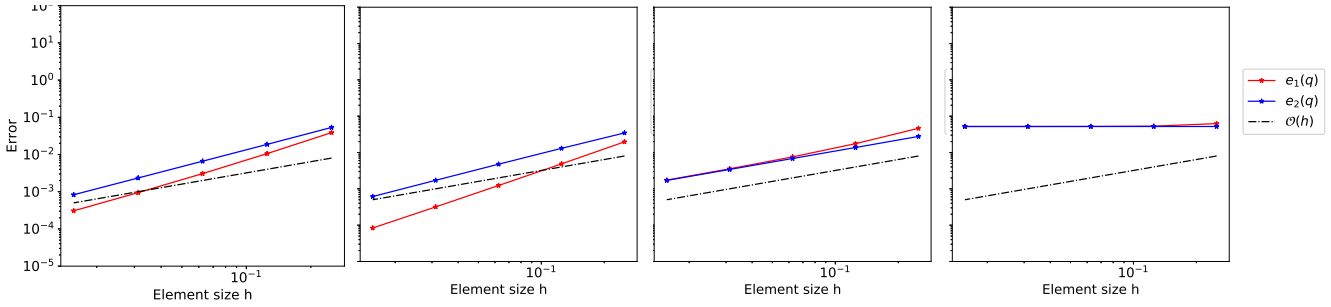

$\nu = \pi/4$ - STE (TH) $\nu = \pi/4$ - STE (PSPG) $\nu = \pi/4$ - PPEvisc $\nu = \pi/4$ - PPE

Figure 7: Pressure error curves and bounds for viscosities values $\pi/4, \pi/2, \pi$ and 2π of Example 4.

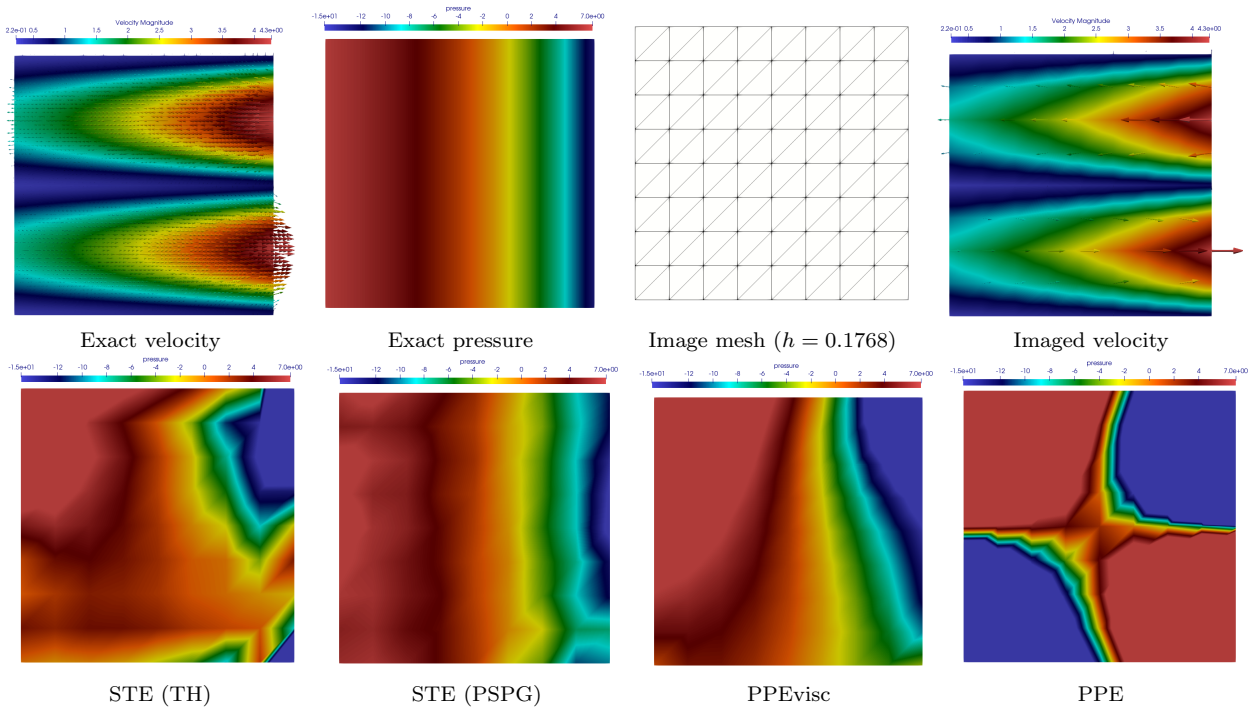

Figure 8: $\mathcal{P}_1$-interpolated reference velocity and pressure fields (top) and reconstructed pressure fields with order $k = 1$ (bottom) for $\nu = 2\pi$ in Example 4.

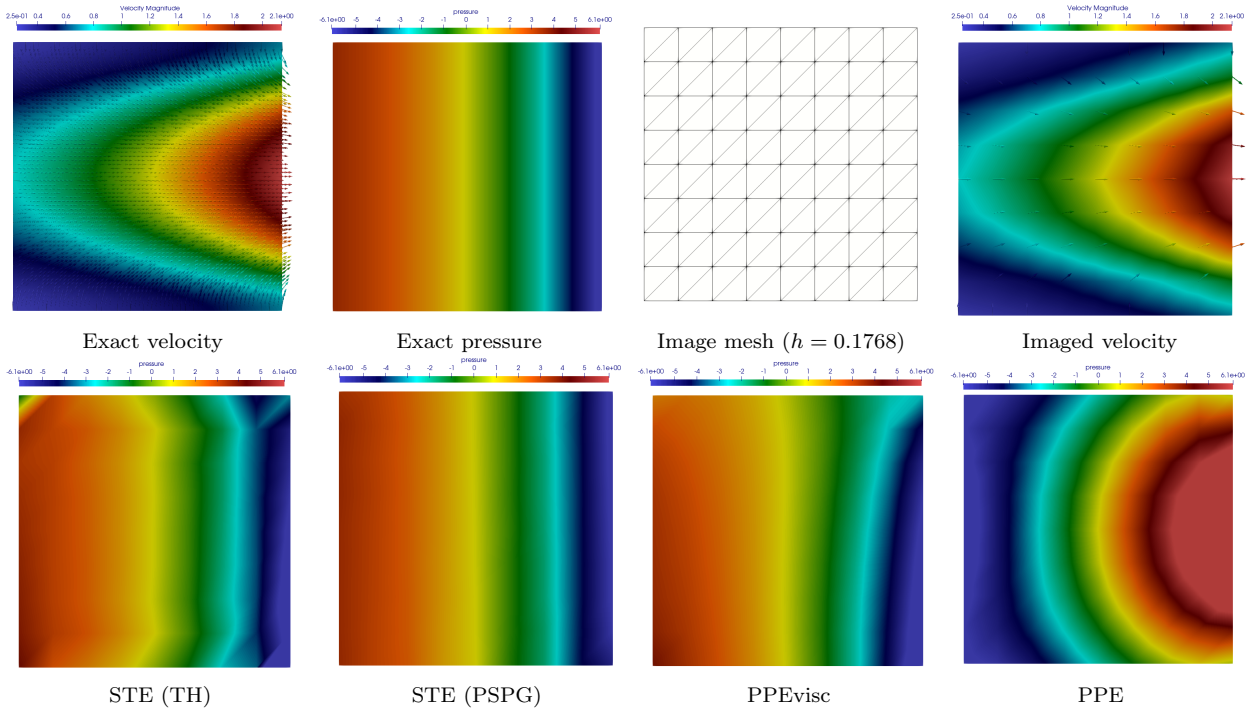

Figure 9: $\mathcal{P}_1$-interpolated reference velocity and pressure fields (top) and reconstructed pressure fields with order $k = 1$ (bottom) for $\nu = \pi$ in Example 4.

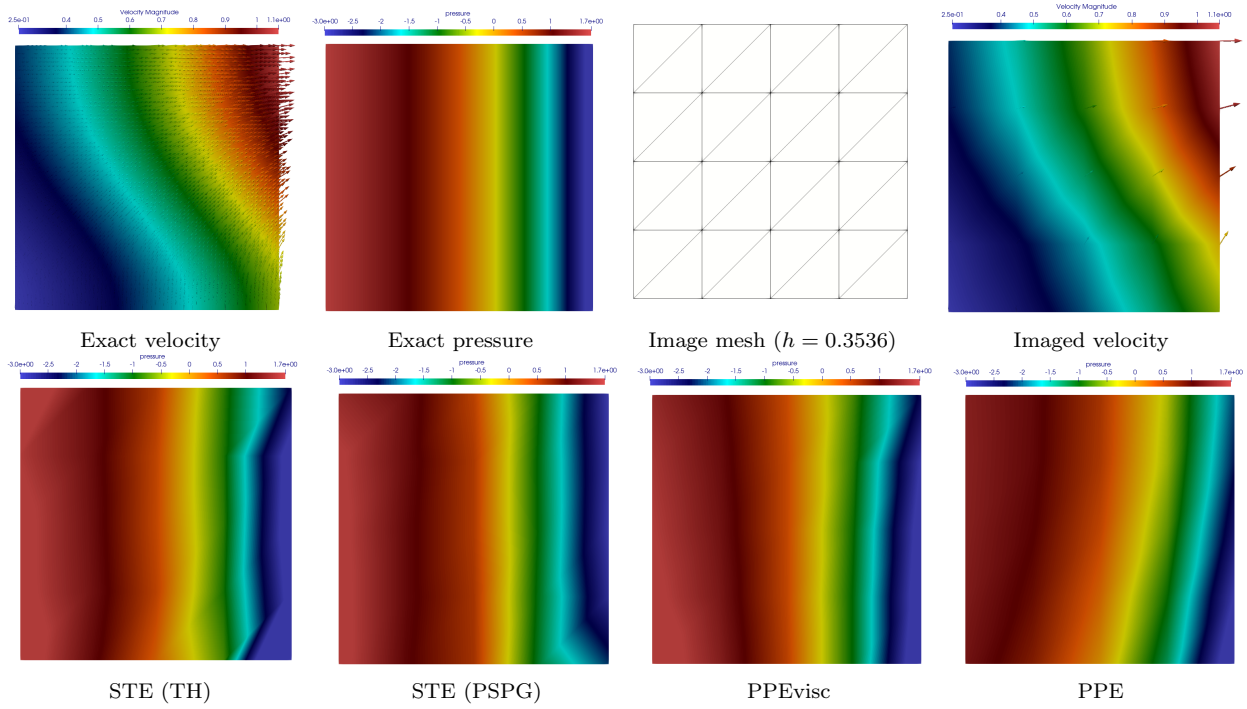

Figure 10: $\mathcal{P}_1$-interpolated reference velocity and pressure fields (top) and reconstructed pressure fields with order $k = 1$ (bottom) for $\nu = \pi/2$ in Example 4.

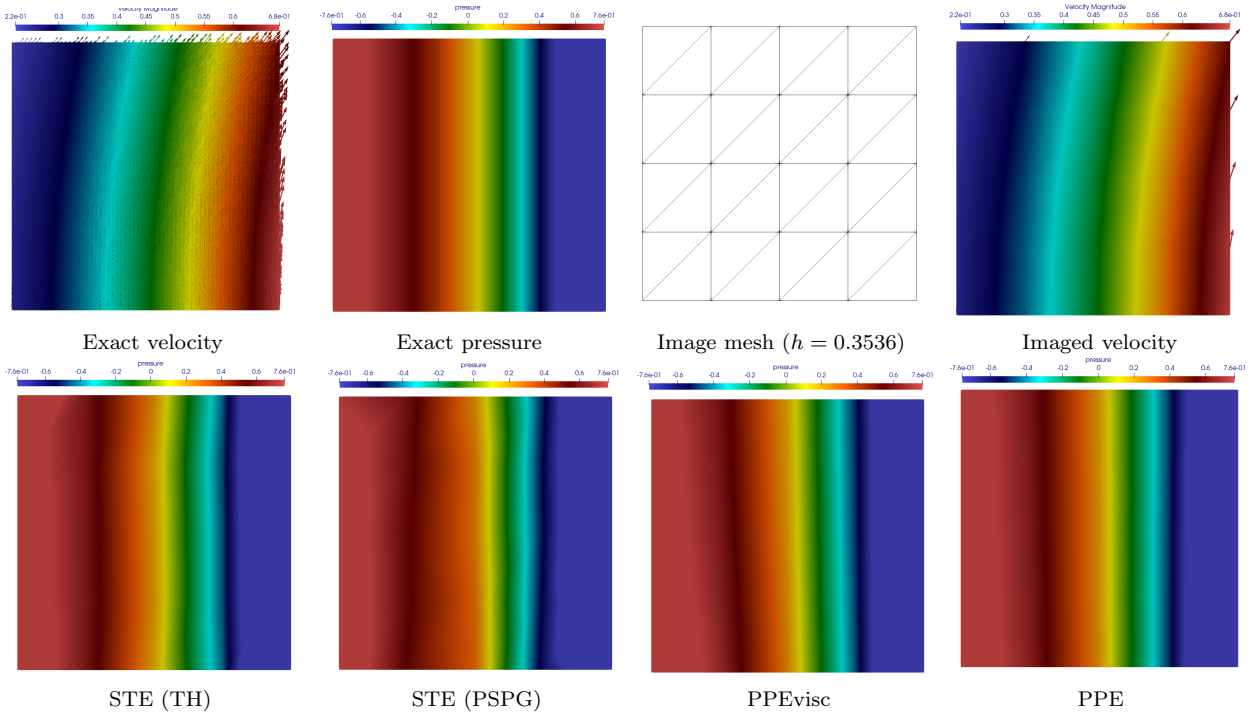

Figure 11: $\mathcal{P}_1$-interpolated reference velocity and pressure fields (top) and reconstructed pressure fields with order $k = 1$ (bottom) for $\nu = \pi/4$ in Example 4.

5. Computations using experimental MRI data

Experimental MRI data was used to assess the impact of discretization in the pressure estimation methods in realistic data and flow regimes. The setup consisted of a 3D printed, MR compatible phantom of the thoracic aorta with 60 % of obstruction in order to produce a typical obstruction. A blood mimicking fluid was pumped into the phantom obtaining physiological velocities. The phantom was equipped with a catheterization unit to measure invasively and simultaneously the pressure gradient across the obstruction. 4D Flow MRI was acquired with an isotropic voxel size of 0.9 mm and 25 time instants along the emulated cardiac cycle. We refer to [21, 12, 13] for the technical details of the experiment. The 4D Flow data is shown in Figure 1.

Two tetrahedral meshes for the pressure computations were constructed. The first one was created using the original 0.9 mm resolution where the nodes of the mesh correspond to the voxels center. The second mesh has 2 mm resolution created using linear interpolation on the first mesh.

Pressure maps were computed from all 4D Flow data sets with the PPE, PPEvisc and STE methods. Due to the pulsatile nature of the experiment, the term

$$-(\partial_\tau \boldsymbol{u}, \nabla r)_\Omega \text{ and } -(\partial_\tau \boldsymbol{u}, r)_\Omega,$$

with ∂_τ the backward finite difference operator between two measured time instants, were added to the right-hand-side of the PPE and STE methods, respectively. This implies that the convergence analysis does not fully apply to the this experimental setup, however, the goal is merely to give an idea on how the discretization setup and methods compare in a scenario of practical relevance.

The pressure differences, to be compared with the corresponding catheter values, were defined as differences of the pressure averages over two spheres with a radius of 4 mm at locations proximally (ascending aorta) and distally to the obstruction.

For the PPE and PPEvisc continuous Galerkin finite elements with $k = 1, 2, 3$ were considered.

For the STE, both Taylor-Hood (TH) and PSPG cases were computed, the latter with stabilization parameter $\delta = 0.01$ as in the previous section for the convergence analysis. In the 2 mm element size mesh, $k = 1, 2$ was tested for both TH and PSPG. In the 0.9 mm element size mesh, only $k = 1$ was used for TH (due to the very high computational cost of higher order) and $k = 1, 2$ was used for PSPG. These methods were implemented using the FEM library FEniCS [1].

Figure 12 shows the results of the pressure estimation, where the catheter pressure values show that the 4D Flow based pressure estimation deliver reasonable values. However, note that the catheter measurements cannot be considered as ground truth, since the precision of the pressure measurements can be considered within a few mmHg [13, 4, 24]. It can be noted that:

- PPE and PPEvisc deliver visually the same results, which may occur due to the fact that viscous effects are negligible in this type of (patho-)physiological flows.
- PPE and PPEvisc allow for a larger pressure gradient when increasing k in the coarse mesh.
- PPE and PPEvisc are less sensitive to k for the finest mesh.
- STE methods allow to recover larger pressure differences than PPE methods.
- STE-PSPG delivers equal or better results than STE-TH for $k = 1$, what is consistent with the convergence results of the numerical tests in the previous section.
- STE-PSPG seems not to profit from increasing polynomial order, what is consistent with convergence results for high Reynolds numbers.
- If one may take the catheter measurements as a ground truth, STE-PSPG would deliver the most accurate results.

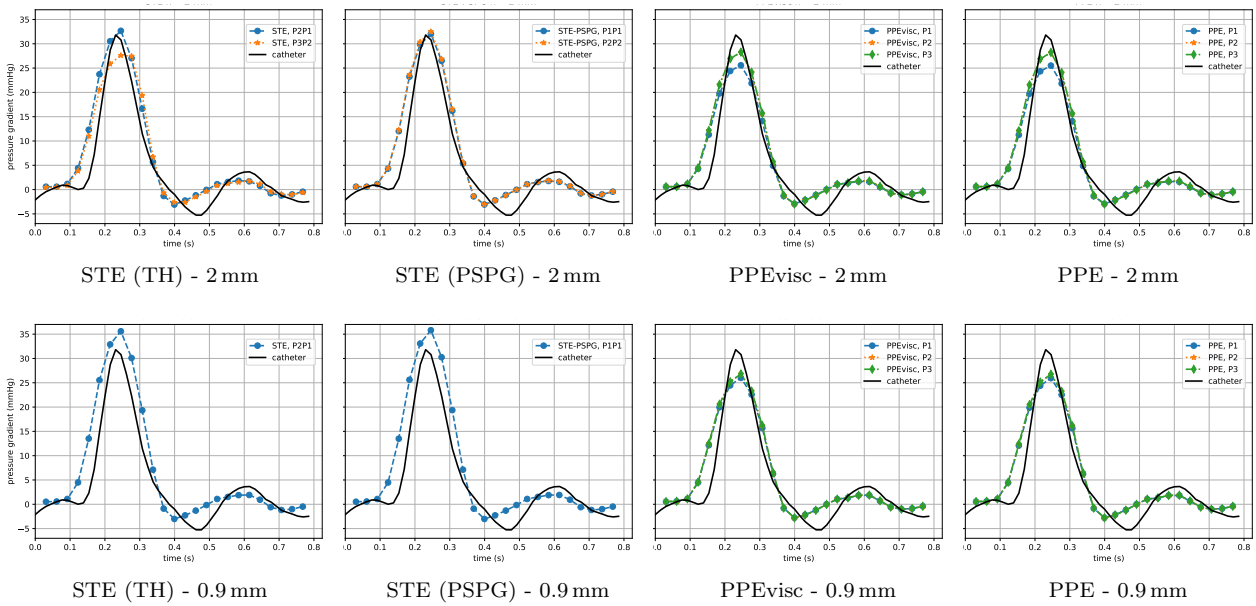

STE (TH) - 2 mm | STE (PSPG) - 2 mm | PPEvisc - 2 mm | PPE - 2 mm

STE (TH) - 0.9 mm | STE (PSPG) - 0.9 mm | PPEvisc - 0.9 mm | PPE - 0.9 mm

Figure 12: Pressure difference in the obstruction over time error computed from 4D Flow and compared with the catheter values.

6. Conclusions

In this article we have analyzed theoretically and numerically some strategies used to recover pressure fields from discrete velocities using the incompressible Navier-Stokes equations.
We analyze two methods, the STE and PPE. While the STE is implemented using the classical Taylor-Hood finite element spaces and pressure-stabilizing Petrov-Galerkin (PSPG), the PPE is implemented with the traditional continuous Galerkin method. For the PPE, two versions have been studied, the standard one without (the viscous term) and a modified one including the viscous term.
The error analysis shows that all methods, except the standard PPE, converge to the exact solution when decreasing the element size of the image mesh h.With respect to the convergence rate, terms of several orders appear in the error analysis. Numerical results show that for the PPEvisc linear order dominates in the presented test cases. For the STE, convergence in the numerical examples vary depending on the testcase and the polynomial order.
Numerical results in academic test cases show that with increasing Reynolds number, the results appear to be less sensitive to an increase in polynomial order, in particular for the STE while the PPEvisc shows some improvements. In many of the cases, the error also appears to decrease faster with h for the STE than the PPEvisc. Among both STE discretizations, PSPG appears to be equally or sometimes more accurate than Taylor-Hood approximations.
The computations with real MRI data are aligned with these observations. Therefore, it appears that STE-PSPG can be the method of choice with the best accuracy and reasonable computational cost.

Acknowledgements

The authors would like to thank to Douglas Pachecho, Institute of Computational Mathematics, TU Graz, Austria, for the discussions about the PPE and to Abner Poza, Dept. of Mathematics and Applied Physics, UCSC, Chile, for the suggestions received.
R.A. was partially supported by ANID-Chile through the projects Centro de Modelamiento Matemático (AFB170001) of the PIA Program: Concurso Apoyo a Centros Científicos y Tecnológicos de Excelencia

con Financiamiento Basal, and FONDECYT project 1211649. C.B. received funding from the European Research Council (ERC) under the European Union's Horizon 2020 research and innovation programme (grant agreement No852544 - CardioZoom). C.C. was partially supported by ANID-Chile through scholarship PCHA/Doctorado Nacional. S.U. acknowledges funding from the Millennium Nucleus for Cardiovascular Magnetic Resonance and FONDECYT grant 1181057.

References

[1] Alnæs, M., Blechta, J., Hake, J., Johansson, A., Kehlet, B., Logg, A., Richardson, C., Ring, J., Rognes, M.E., Wells, G.N., 2015. The FEniCS Project Version 1.5. Archive of Numerical Software 3. doi:10.11588/ans.2015.100.20553.

[2] Baumgartner, H., Bonhoeffer, P., De Groot, N.M., de Haan, F., Deanfield, J.E., Galie, N., Gatzoulis, M.A., Gohlke-Baerwolf, C., 2010. ESC Guidelines for the management of grown-up congenital heart disease (new version 2010) The Task Force on the Management of Grown-up Congenital Heart Disease of the European Society of Cardiology (ESC). European heart journal 31, 2915–2957.

[3] Bertoglio, C., Núñez, R., Galarce, F., Nordsletten, D., Osses, A., 2017. Relative pressure estimation from velocity measurements in blood flows: State-of-art and new approaches. Int. J. Numer. Meth. Biomed. Engng. 34. URL: https://doi.org/10.1002/cnm.2925.

[4] Brüning, J., Hellmeier, F., Yevtushenko, P., Kühne, T., Goubergrits, L., 2018. Uncertainty quantification for non-invasive assessment of pressure drop across a coarctation of the aorta using CFD. Cardiovascular engineering and technology 9, 582–596.

[5] Di Pietro, D., Ern, A., 2012. Mathematical Aspects of Discontinuous Galerkin Methods. Springer-Verlag Berlin Heidelberg. doi:10.1007/978-3-642-22980-0.

[6] Ebbers, T., Wigström, L., Bolger, A., Engvall, J., Karlsson, M., 2001. Estimation of relative cardiovascular pressure using time-resolved three-dimensional phase contrast mri. Magn. Reson. Med 45, 872–879. doi:10.1002/mrm.1116.

[7] Ern, A., Guermond, J., 2004. Theory and Practice of Finite Elements. Springer New York. doi:10.1007/978-1-4757-4355-5.

[8] Girault, V., Raviart, P., 1986. Finite element methods for Navier-Stokes equations: Theory and Algorithms.. volume 5 of *Springer Series in Computational Mathematics*. Springer-Verlag. doi:10.1007/978-3-642-61623-5.

[9] Guermond, J., Minev, P., Shen, J., 2006. An overview of projection methods for incompressible flows. Comput. Methods Appl. Mech. Engrg. 195, 6011–6045. doi:10.1016/j.cma.2005.10.010.

[10] Hugues, T., Franca, L., Balestra, M., 1986. A new finite element formulation for computational fluis dynamics: V. Circumventing the Babuska-Brezzi condition: A stable Petrov-Galerkin formulation of the Stokes problem accommodating equal-order interpolations. Comput Methods. Appl. Mech. Engrg. 59, 85–99. doi:10.1016/0045-7825(86)90025-3.

[11] Markl, M., Frydrychowicz, A., Kozerke, S., Hope, M., Wieben, O., 2012. 4D flow MRI. Journal of Magnetic Resonance Imaging 36, 1015–1036.

[12] Montalba, C., Urbina, J., Sotelo, J., Andia, M.E., Tejos, C., Irarrazaval, P., Hurtado, D.E., Valverde, I., Uribe, S., 2018. Variability of 4D flow parameters when subjected to changes in MRI acquisition parameters using a realistic thoracic aortic phantom. Magnetic resonance in medicine 79, 1882–1892.

[13] Nolte, D., Urbina, J., Sotelo, J., Sok, L., Montalba, C., Valverde, I., Osses, A., Uribe, S., Bertoglio, C., 2021. Validation of 4d flow based relative pressure maps in aortic flows. Medical Image Analysis 74, 102195. doi:https://doi.org/10.1016/j.media.2021.102195.

[14] Omran, H., Schmidt, H., Hackenbroch, M., Illien, S., Bernhardt, P., von der Recke, G., Fimmers, R., Flacke, S., Layer, G., Pohl, C., 2003. Silent and apparent cerebral embolism after retrograde catheterisation of the aortic valve in valvular stenosis: A prospective, randomised study. The Lancet 361, 1241–1246.

[15] Ozisik, S., Riviere, B., Warburton, T., 2010. On the Constants in the Inverse Inequalities in L^2. Technical Report. Rice University, https://hdl.handle.net/1911/102161.

[16] Pacheco, D., Steinbach, O., 2020. A continuous finite element framework for the pressure poisson equation allowing non-newtonian and compressible flow behavior. Int. J. Numer. Meth. Fluids , 1 – 11doi:10.1002/fld.4936.

[17] Rhebergen, S., Wells, G., 2018. A hybridizable discontinuous galerkin method for the navier–stokes equations with pointwise divergence-free velocity field. J Sci Comput 76, 1484–1501. doi:10.1007/s10915-018-0671-4.

[18] Smith, N., et al., 2012. A finite-element approach to the direct computation of relative cardiovascular pressure from time-resolved mr velocity data. Medical Image Analysis 16, 1029–1037. doi:10.1016/j.media.2012.04.003.

[19] Soulat, G., McCarthy, P., Markl, M., 2020. 4d flow with mri. Annual Review of Biomedical Engineering 22. doi:10.1146/annurev-bioeng-100219-110055.

[20] Steinbach, O., 2008. Numerical Approximation Methods for Elliptic Boundary Value Problems: Finite and Boundary Elements. Springer, New York. doi:10.1007/978-0-387-68805-3.

[21] Urbina, J., Sotelo, J.A., Springmüller, D., Montalba, C., Letelier, K., Tejos, C., Irarrázaval, P., Andia, M.E., Razavi, R., Valverde, I., Uribe, S.A., 2016. Realistic aortic phantom to study hemodynamics using MRI and cardiac catheterization in normal and aortic coarctation conditions. Journal of Magnetic Resonance Imaging 44, 683–697. doi:10.1002/jmri.25208.

[22] Švihlová, H., Hron, J., Málek, J., Rajagopoal, K., Rajagopoal, K., 2016. Determination of pressure data from velocity data with a view toward its application in cardiovascular mechanics. part 1. theoretical considerations. Int. J. of Eng. Sci. 105, 108–127. doi:10.1016/j.ijengsci.2015.11.002.

[23] Vahanian, A., et al., 2012. Guidelines on the management of valvular heart disease (version2012). European Heart Journal 19, 2451–2496. doi:10.1093/eurheartj/ehs109.

[24] de Vecchi, A., Clough, R.E., Gaddum, N.R., Rutten, M.C., Lamata, P., Schaeffter, T., Nordsletten, D.A., Smith, N.P., 2014. Catheter-induced errors in pressure measurements in vessels: an in-vitro and numerical study. IEEE Transactions on Biomedical Engineering 61, 1844–1850.

[25] Vitiello, R., McCrindle, B.W., Nykanen, D., Freedom, R.M., Benson, L.N., 1998. Complications associated with pediatric cardiac catheterization. Journal of the American College of Cardiology 32, 1433–1440.

[26] Warburton, T., Hesthaven, J.S., 2003. On the constants in hp-finite element trace inverse inequalities. Comput. Methods Appl. Mech. Engrg. 1 192, 2765–2773. doi:10.1016/S0045-7825(03)00294-9.

[27] Wyman, R.M., Safian, R.D., Portway, V., Skillman, J.J., McKAY, R.G., Baim, D.S., 1988. Current complications of diagnostic and therapeutic cardiac catheterization. Journal of the American College of Cardiology 12, 1400–1406.